Argonne
NATIONAL LABORATORY

Generation IV Nuclear Energy System Initiative Large GFR Core Subassembly Design for the Gas-Cooled Fast Reactor

Nuclear Engineering Division

Generation IV Nuclear Energy System Initiative

Large GFR Core Subassembly Design for the Gas-Cooled Fast Reactor

by
E. E. Feldman
E. A. Hoffman
R. F. Kulak
I. U. Therios
T. Y. C. Wei

Nuclear Engineering Division, Argonne National Laboratory

August 2005

Table of Contents

List of Figures

List of Tables

1. Introduction

Gas-cooled fast reactor (GFR) designs are being developed to meet Gen IV goals of sustainability, economics, safety and reliability, and proliferation resistance and physical protection as part of an International Generation IV Nuclear Energy System Research Initiative effort. Different organizations are involved in the development of a variety of GFR design concepts. The current analysis has focused on the evaluation of low-pressure drop, pin-core designs with favorable passive cooling properties. Initial evaluation of the passive cooling safety case for the GFR during depressurized decay heat removal accidents with concurrent loss of electric power have resulted in requirements for a reduction of core power density to the 100 w/cc level and a low core pressure drop of 0.5 bars. Additional design constraints and the implementation of their constraints are evaluated in this study to enhance and passive cooling properties of the reactor.

Passive cooling is made easier by a flat radial distribution of the decay heat. One goal of this study was to evaluate the radial power distribution and determine to what extent it can be flattened, since the decay heat is nearly proportional to the fission power at shutdown. In line with this investigation of the radial power profile, an assessment was also made of the control rod configuration. The layout provided a large number of control rod locations with a fixed area provided for control rods. The number of control rods was consistent with other fast reactor designs. The adequacy of the available control rod locations was evaluated. Future studies will be needed to optimize the control rod designs and evaluate the shutdown system.

The case for low pressure drop core can be improved by the minimization of pressure drop sources such as the number of required fuel spacers in the subassembly design and by the details of the fuel pin design. The fuel pin design is determined by a number of neutronic, thermal-hydraulic (gas dynamics) and fuel performance considerations. For the purposes of this study, the starting point is the fuel pin design established by the CEA-ANL/US I-NERI collaboration project for the selected 2400 MWt large rector option. Structural mechanics factors are now included in the design assessment. In particular, thermal bowing establishes a bound on the minimum of fuel pin spacers required in each fuel subassembly to prevent the local flow channel restrictions and pin-to-pin mechanical interaction. There are also fabrication limitations on the maximum length of SiC fuel pin cladding which can be manufactured. This geometric limitation effects the minimum ceramic clad thickness which can be produced. This ties into the fuel pin heat transfer and temperature thresholds. All these additional design factors were included in the current iteration on the subassembly design to produce a lower core pressure drop. A more detailed definition of the fuel pin/subassembly design is proposed here to meet these limitations.

This subassembly design was then evaluated under low pressure natural convection conditions to assess its acceptability for the decay heat removal accidents. A number of integrated decay heat removal (DHR) loop plus core calculations were performed to scope the thermal-hydraulic response of the subassembly design to the accidents of

interest. It is evident that there is a large sensitivity to the guard containment back pressure for these designs. The implication of this conclusion and possible design modifications to reduce this sensitivity will be explored under the auspices of the International GENIV GFR collaborative R&D plan.

Chapter 2 describes the core reference design for the 2,400 MWt GFR being evaluated. The methodology, modeling, and codes used in the analysis of the fuel pin structural behavior are described in Chapter 3. Chapter 4 provides the result of the thermal-hydraulic study of the assembly design for the accidents of interest. An evaluation of the performance and control rod reactivity control is also presented in Chapter 2.

2. Core Neutronics Design

2.1 Reference Case

The reference design is a 2400 MWt pancake (H/D ~ 0.28) core. The conversion ratio was approximately 1.0 for the three-batch scatter loading with an average 10% discharge burnup. The equilibrium-recycle fuel cycle was analyzed. Since the conversion ratio was maintained at unity, all the TRU is supplied from recycled fuel. The makeup uranium was depleted uranium. The core consists of 366 fuel (271 fuel pins) assemblies, 54 fuel assemblies (234 fuel pins) with a central control rod, and 7 fuel assemblies (234 fuel pins) with a central shutdown rod. Figure 2.1 shows the reactor layout for the reference design.

The assembly design included both fuel and control assemblies as indicated above. The fuel pins in all assemblies are the same design. The control assemblies have a centrally located control tube which replaces 37 of the fuel pins. The details of the reference assembly design are provided in Table 2.1.

The reference fuel cycle is a scatter-load 3-batch core with recycle. The TRU enrichment (TRU/HM) was adjusted to achieve the targeted cycle length. The goal of this study was to flatten the radial power distribution relative to the reference loading. Fuel loading options including enrichment splitting, fuel shuffling were considered. An annular core design was evaluated with and without enrichment splitting. The power distribution of a 600 MWt design is provided for comparison.

The conversion ratio and average discharge burnup remained fixed for the different design variants. The fuel pin diameter was adjusted to maintain a conversion ratio equal to unity. Variations in pin diameter change the fuel loading and average discharge burnup. The cycle length was adjusted to compensate and maintain the average discharge burnup at 10%. None of the designs required significant changes to maintain these parameters.
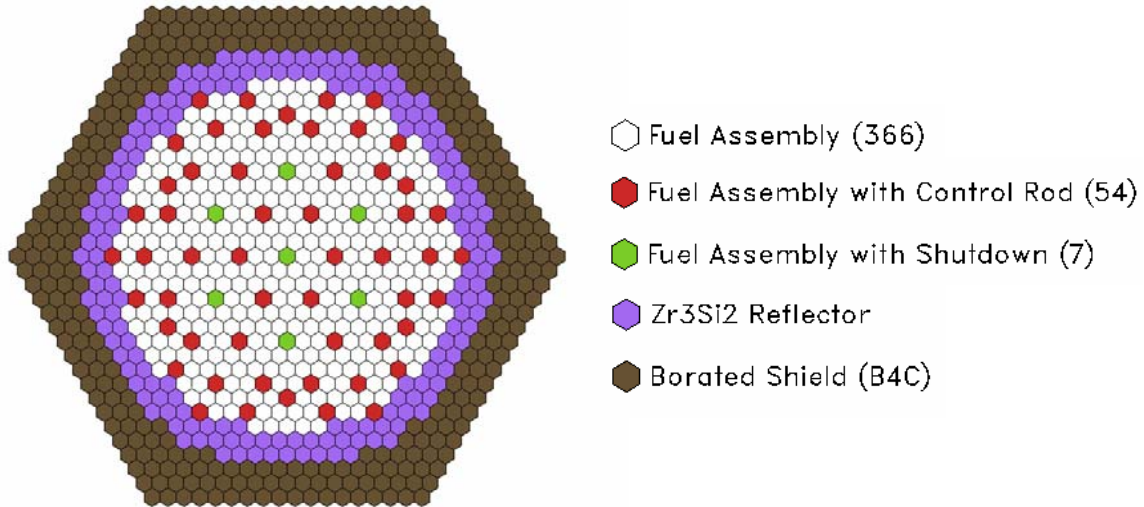
Figure 2.1. Reference Reactor Layout.

Table 2.1. Equilibrium TRU Breakeven Gas-Cooled Fast Reactor Designs.

Assembly Type	Fuel	Control	Reflector	Shield
Assembly Pitch (mm)	222	222	222	222
Assembly Flat-to-Flat (mm)	215	215	215	215
Duct Thickness (mm)	3.7	3.7	3.7	3.7
Duct Material	SiC	SiC	Zr_3Si_2	W
Pins	271	234	19	19
Pin Diameter (mm)	9.57	9.57	40.1	40.1
Clad Thickness (mm)	1.00	1.00	N/A	0.019
Clad Material	SiC	SiC	N/A	W
Pellet Outer Diameter (mm)	7.37	7.37	N/A	38.9
Pellet Inner Diameter (mm)	3.02	3.02	N/A	N/A
Pellet Material	(U,TRU)C	(U,TRU)C	Zr_3Si_2	B_4C
Control Rod Outer Diameter (mm)	N/A	80.5	N/A	N/A
Control Rod Cladding Thickness (mm)	N/A	1	N/A	N/A
B_4C Diameter (mm)	N/A	78.5	N/A	N/A

2.2 **Fuel Cycle and Neutronics Modeling**

Full-core, equilibrium-cycle calculations were performed using the REBUS-3 fuel cycle analysis code [2.1]. An enrichment search was performed to determine the TRU enrichment required to achieve an end of equilibrium cycle (EOEC) unpoisoned k_{eff}=1.0. An external cycle time of three years and 0.1% losses of the actinides were assumed.

Region-dependent 33-group cross sections were generated with the MC^2-2 code [2.2] based on ENDF/B-V nuclear data. Beginning of cycle material compositions and temperatures from the reference design were used to generate the cross section library. The flux distributions were obtained using the nodal diffusion theory option of the DIF3D code [2.3].

4

A number of reactivity parameters were calculated by using the beginning of equilibrium cycle (BOEC) and EOEC number densities from the REBUS-3 calculations, generating individual finite-difference DIF3D cases, and new cross section sets using MC^2-2 for the reference conditions and the perturbed conditions. The values were calculated by eigenvalue difference. This was done with the exception of the axial and radial expansion calculations, where the unperturbed BOEC or EOEC cross section library was used. The delayed neutron fraction and prompt neutron lifetime were calculated at the BOEC and EOEC with VARI3D [2.4] using the real and adjoint fluxes calculated with DIF3D for the unperturbed conditions.

The reactivity effect of a depressurization accident was evaluated. The coolant pressure was assumed to fall instantaneously to atmospheric pressure throughout the system. New coolant number density was calculated at one atmosphere using the ideal gas law. The reactivity effect of instantaneous depressurization was evaluated at BOEC and EOEC.

For the expansion cases, the core volume is increased 5% by either radial or axial expansion. The number densities, except for the coolant, were reduced to conserve mass. The coolant number densities remained constant.

2.3 Radial Power Distribution

The primary goal was to estimate the minimum radial assembly peaking factor. The primary motivation for flattening the power distribution is passive cooling after shutdown. The decay heat is roughly proportional to the power at shutdown, but other factors such as burnup, TRU enrichment, and isotopics have significant impacts on the actual decay heat production as a function of time after shutdown. These secondary effects would need to be evaluated in order to accurately estimate the assembly power sharing after shutdown.

There are a large number of options for flattening the radial power distribution. A number of these options were explored. The design variants were not completely optimized, but significant further reductions in the peaking factor are not likely. Each option was considered independently. Power redistribution limited the ability to flatten the power distribution. Shorter cycle lengths would limit this effect, but were not analyzed. The power distribution map is a color-coded sixth core map. The peak to average assembly power density for each assembly is provided with colors split into seven color-coded groups: >1.4 in red; >1.2 in orange; >1.05 in gold; >0.95 in yellow; >0.8 in light green; >0.4 in sky blue; <0.4 in blue; and black for the non-fuel assemblies. The fuel assemblies are normalized to the average power density in the fueled portion of the assembly. This corrects for the central control assembly in the control and shutdown assemblies.

2.3.1 Uniform Initial Enrichment

The initial case evaluated was for the reference design. This design has a uniform TRU enrichment and a scatter loading pattern. Assembly by assembly modeling would be too time consuming at this stage of design. The core model has radial and axial depletion

zones with homogeneous compositions. This results in each assembly in a zone having the same composition, which includes equal fractions of fresh, once-burned, and twice-burned fuel. Therefore, differences in power sharing within a zone resulting from depletion are not modeled, but the conversion ratio of unity and the fast spectrum will limit the impact of this modeling approximation.

Figures 2.2 to 2.4 show the radial power distribution for BOEC, MOEC, and EOEC, respectively. The results show a large peak to average power of 1.74 at BOEC. There is very little power redistribution over the cycle with the peak to average power being 1.62 at EOEC with the peak still located at the center.

2.3.2 Out to In Fuel Shuffle

The first methodology used to reduce the power peaking was to evaluate an out-to-in fuel shuffle. The number of fuel batches was increased from three to four and the central shutdown assembly was unfueled to make an integer number of fuel assemblies in each batch and to reduce the central peaking factor.

Figures 2.5 to 2.7 show the radial power distribution for BOEC, MOEC, and EOEC, respectively. The results show a large peak to average power of 1.57 at BOEC. There is very little power redistribution over the cycle with the peak to average power being 1.47 at EOEC with the peak still located near the center. The conversion ratio of unity leads to very little change in reactivity as the fuel assemblies are depleted. Therefore, fuel shuffling appears to have limited ability to flatten the profile for this system.

2.3.3 Non-Uniform Initial Enrichment (Flat BOEC)

A split-batch fuel loading strategy was evaluated with four different initial enrichments in each batch. The initial enrichment and number of assemblies in each split batch were adjusted to minimize the BOEC peak to average assembly power. Initially, there was no limit on the TRU enrichment, but the conversion ratio was maintained at near unity.

Figures 2.8 to 2.10 show the radial power distribution for BOEC, MOEC, and EOEC, respectively. The results show a large reduction in the peak to average power. At BOEC, the peak to average power was reduced to 1.06. Unfortunately, there is significant power redistribution over the cycle with the peak to average power increasing to 1.25 at EOEC. The power redistributes because the higher enriched assemblies near the periphery are burning TRU, which lowers their reactivity over their lifetime, while the lower enriched assemblies near the center are breeding TRU and increasing in reactivity over their lifetime. The net effect of this TRU burning and breeding is a core that remains a TRU breakeven core, but the power as well as the TRU redistributes from the high-enriched assemblies near the periphery to the low enriched assemblies near the center.

The results are not fully optimized, but show that even if a perfectly uniform power distribution were achieved at BOEC, the power would quickly shift towards the center. By MOEC, the peak has increased to 1.17 from 1.06 at BOEC. This suggests that even a reduction in cycle length by one half would only reduce the peak to approximately 1.1 in an idealized situation.

2.3.4 Non-Uniform Initial Enrichment (No TRU limit)

A split-batch fuel loading strategy was evaluated with five different initial enrichments in each batch. The previous section looked at minimizing the BOEC peak to average assembly power, while this analysis attempted to minimize this parameter for the entire cycle by peaking the power near the periphery of the core and allowing the power to redistribute towards the center of the core. The TRU enrichment is still not limited and the conversion ratio was maintained at near unity.

Figures 2.11 to 2.13 show the radial power distribution for BOEC, MOEC, and EOEC, respectively. The results show a small reduction in the peak to average power relative to the previous case. At BOEC, the peak to average power was 1.15 that is higher than the previous case. There is significant power redistribution over the cycle with the peak to average power decreasing to 1.08 at MOEC and then increasing to 1.18 at EOEC. The maximum peak to average power is 1.18, which is an improvement over the previous case. This is near the limit for this cycle length because the peak of 1.15 near the periphery at BOEC is nearly equal to the peak of 1.18 near the center at EOEC. Any further shifts of power from the center at EOEC to the periphery at the BOEC will simply shift the location and time of the maximum assembly power without reducing the magnitude. The maximum enrichment is 25 w/o TRU/HM, which exceeds the imposed limit of 20%.

2.3.5   Non-Uniform Initial Enrichment

A split-batch fuel loading strategy was evaluated with five different initial enrichments in each batch. The previous section imposed no limit on the maximum TRU enrichment. For this section, the TRU enrichment was limited to 20 w/o TRU/HM and the conversion ratio was maintained at near unity.

Figures 2.14 to 2.16 show the radial power distribution for BOEC, MOEC, and EOEC, respectively. The results show a small increase in the peak to average power relative to the previous case. At BOEC, the peak to average power was 1.10 that is slightly lower than the previous case because the 20% limit prevents pulling the power toward the periphery as effectively as the higher enrichment of the previous case. There is significant power redistribution over the cycle with the peak to average power increasing to 1.17 at MOEC and further increasing to 1.25 at EOEC. The maximum peak to average power is 1.25, which is higher than the previous case.

2.3.6   Annular Core – Uniform Enrichment

Since the high power assemblies are located in the center, an annular core that removes these assemblies would reduce the radial power peaking. The 37 centrally located assemblies had the fuel removed and were replaced with reflector material. To maintain similar power density and core height, 36 reflector assemblies were replaced with fuel assemblies. This design was evaluated for a uniform TRU enrichment with a conversion ratio of unity.

Figures 2.17 to 2.19 show the radial power distribution for BOEC, MOEC, and EOEC, respectively. The annular core shows a large reduction in the peak to average power

relative to the reference design with uniform enrichment. At BOEC, the peak to average power was 1.30, which is significantly lower than the 1.74 value for the reference design. There is very little power redistribution over the cycle with the peak to average power decreasing slightly to 1.28 at EOEC. The advantage of the annular core is that without batch splitting, the power distribution improves significantly and there is very little power redistribution over the cycle. The annular core will have a larger core diameter.

2.3.7   Annular Core – Non-Uniform Enrichment

The power distribution can be improved further by using enrichment splitting. The annular core was evaluated for a split-batch fuel loading strategy with four different initial enrichments limited to 20 w/o TRU/HM.

Figures 2.20 to 222 show the radial power distribution for BOEC, MOEC, and EOEC, respectively.   The enrichment splitting shows a significant improvement over the previous case. At BOEC, the peak to average power was 1.19, which is significantly lower than the 1.30 value for the uniform enrichment case. Even for this enrichment splitting case, there is very little power redistribution over the cycle in the annular core. The maximum peak to average power is 1.19, which is lower than any other case. Despite having the lower peaking factor, the reference core layout was maintained and the annular core is a secondary option.

2.3.8   600 MWt Core

Previous analysis had looked at a variety of design options, including small cores such as the 600MWt design included here. This design was for a uniform-enrichment scatter-loaded core. This design did not include fuel in the control assemblies.

Figures 2.23 to 2.25 show the radial power distribution for BOEC, MOEC, and EOEC, respectively. The results show a much smaller peak to average power of 1.22 for the small core. The large leakage flattens the power distribution for the small core. The large core diameter of the 2400 MWt core and poor (relative to breeding blankets) reflector results in a significant peaking of the radial power distribution. The minimum peaking factor achieved with the split-enrichment fuel loading was only slightly lower than that in the 600 MWt core with a uniform enrichment. This shows that it is simpler to produce a more uniform radial power distribution in the small core.
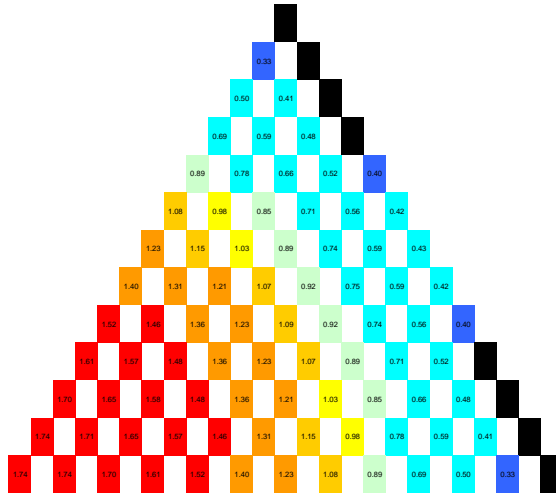
Figure 2.2. Uniform Initial Enrichment – BOEC Radial Power Distribution.
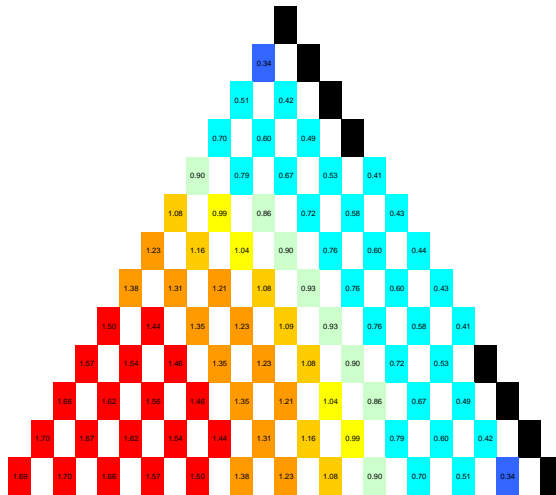
Figure 2.3. Uniform Initial Enrichment – MOEC Radial Power Distribution.
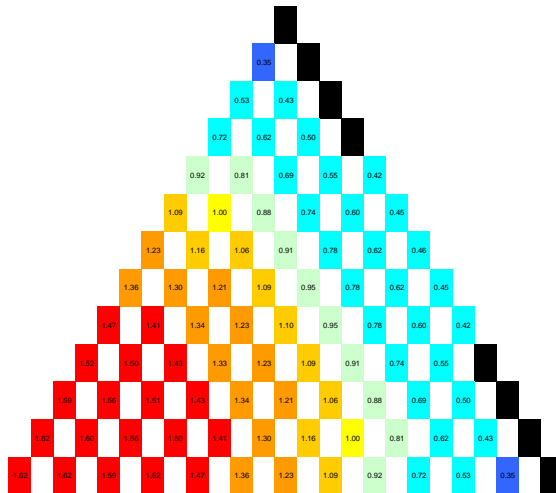
Figure 2.4. Uniform Initial Enrichment – EOEC Radial Power Distribution.
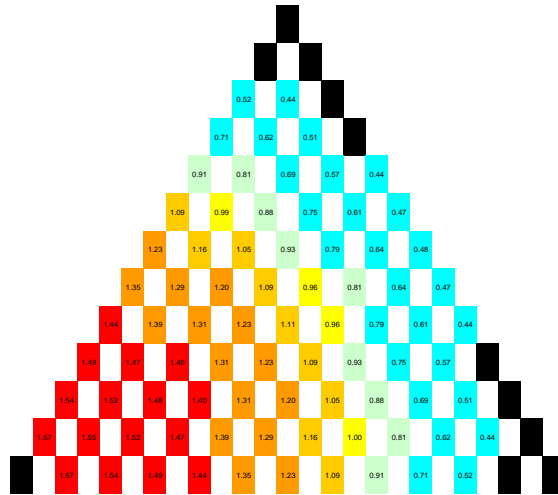
Figure 2.5. Out to In Fuel Shuffle – BOEC Radial Power Distribution.
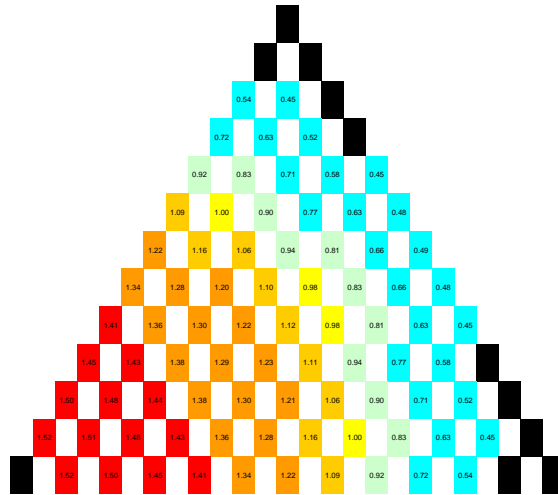
Figure 2.6. Out to In Fuel Shuffle – MOEC Radial Power Distribution.
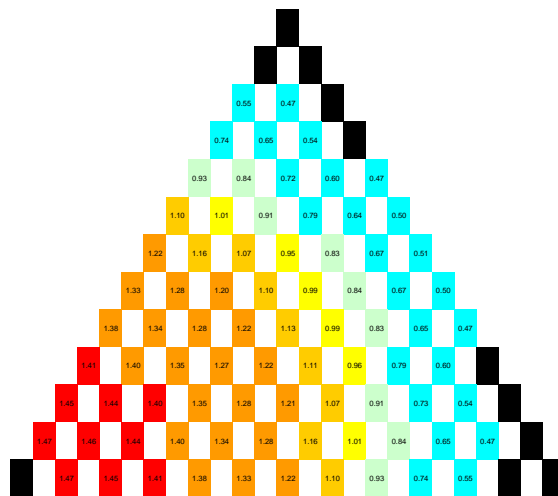
Figure 2.7. Out to In Fuel Shuffle – EOEC Radial Power Distribution.
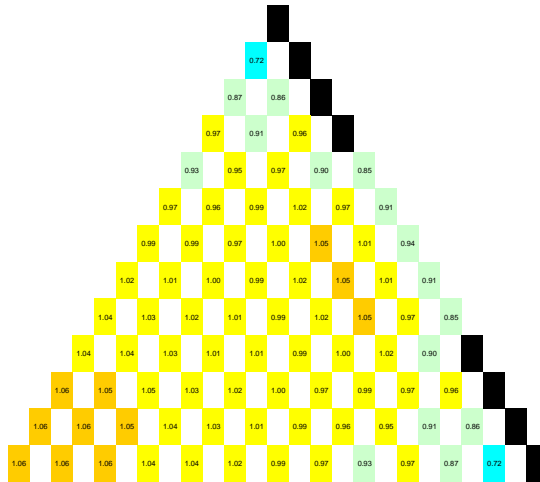
Figure 2.8. Non-uniform Enrichment / Flat BOEC – BOEC Radial Power Distribution.
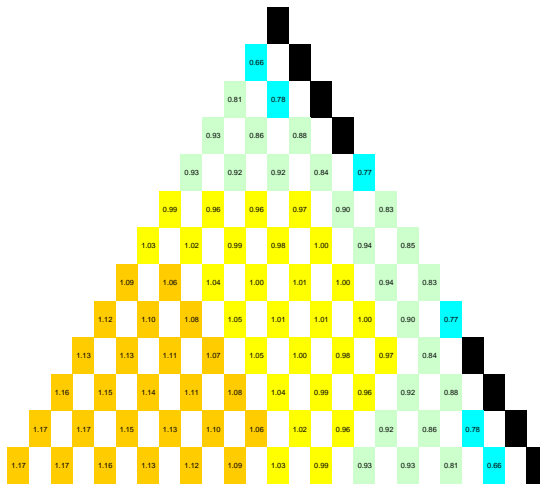
Figure 2.9. Non-uniform Enrichment / Flat BOEC – MOEC Radial Power Distribution.
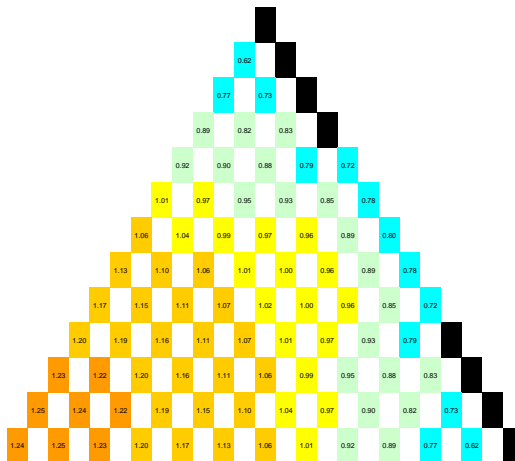
Figure 2.10. Non-uniform Enrichment / Flat BOEC – EOEC Radial Power Distribution.
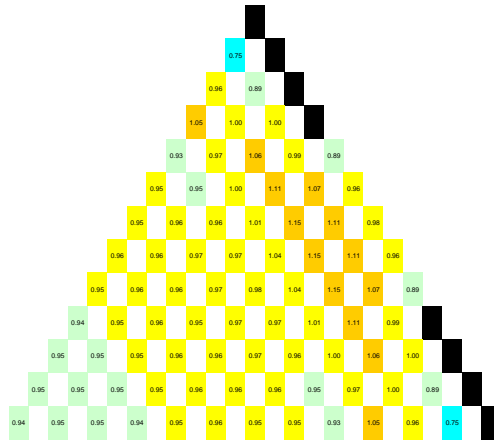
Figure 2.11. Non-uniform Enrichment / No TRU limit – BOEC Radial Power Distribution.
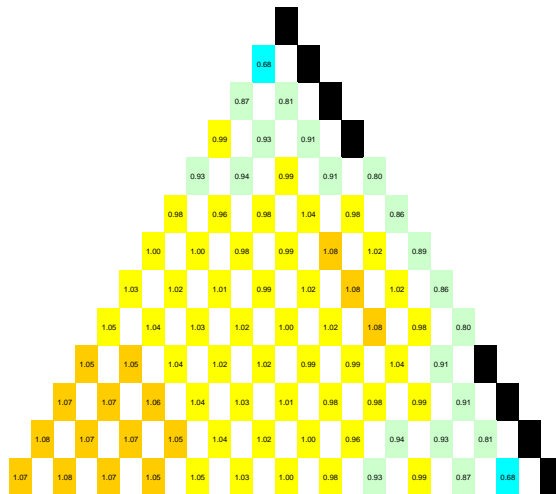
Figure 2.12. Non-uniform Enrichment / No TRU limit – MOEC Radial Power Distribution.
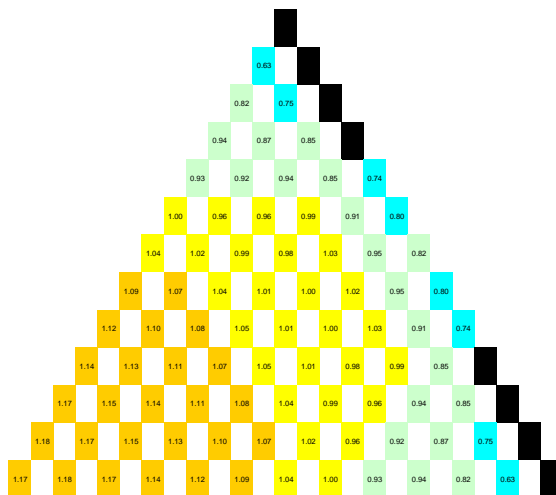
Figure 2.13. Non-uniform Enrichment / No TRU limit – EOEC Radial Power Distribution.
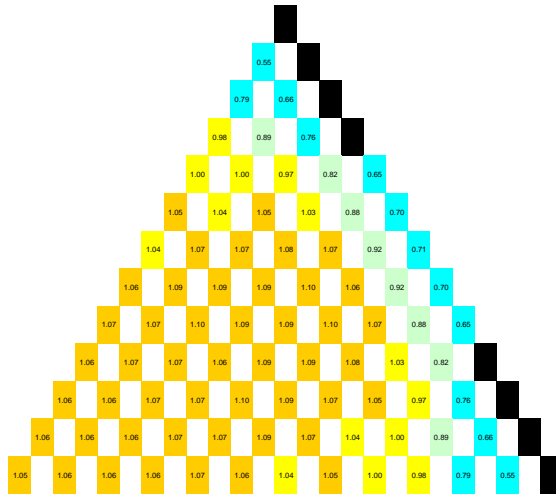
Figure 2.14. Non-uniform Enrichment – BOEC Radial Power Distribution.
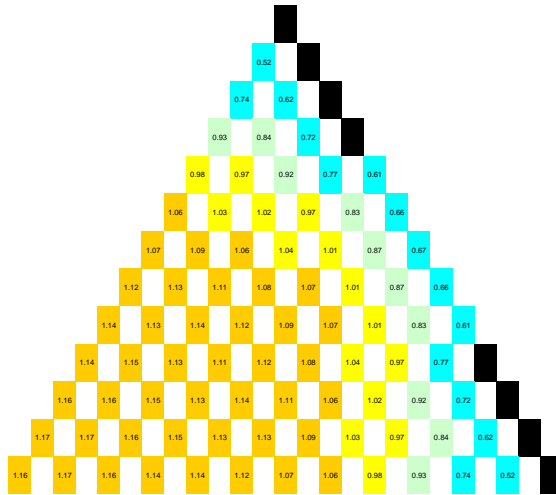
Figure 2.15. Non-uniform Enrichment – MOEC Radial Power Distribution.
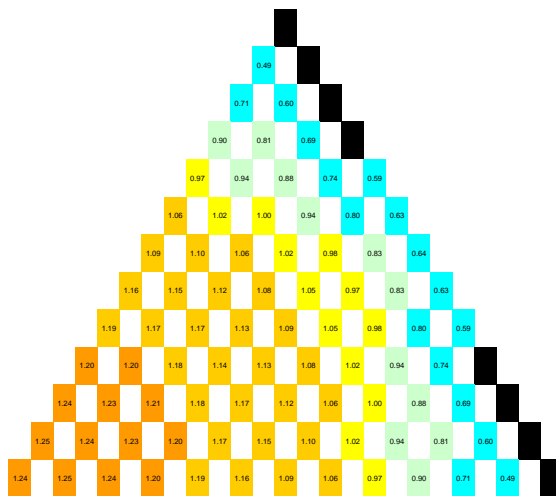
Figure 2.16. Non-uniform Enrichment – EOEC Radial Power Distribution.
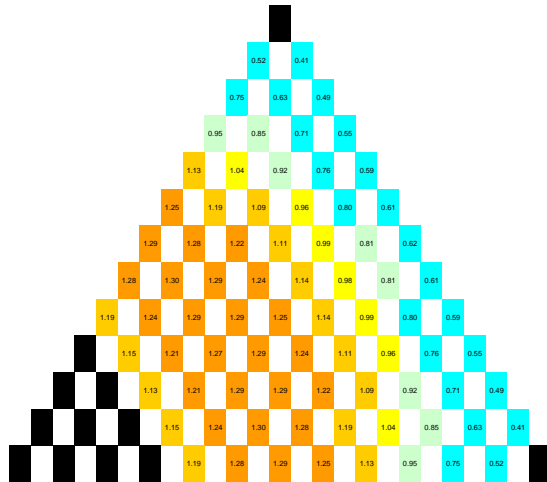
Figure 2.17. Annular Core / Uniform Enrichment – BOEC Radial Power Distribution.
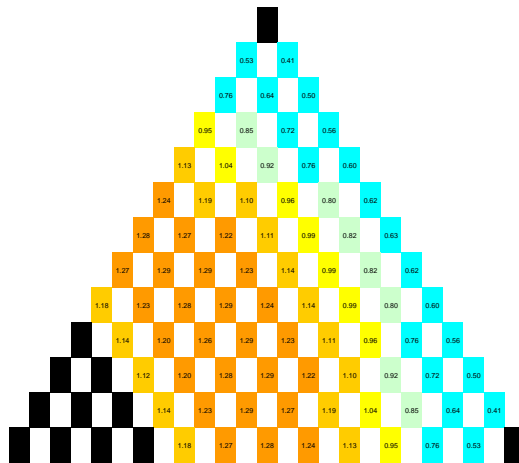
Figure 2.18. Annular Core / Uniform Enrichment – MOEC Radial Power Distribution.
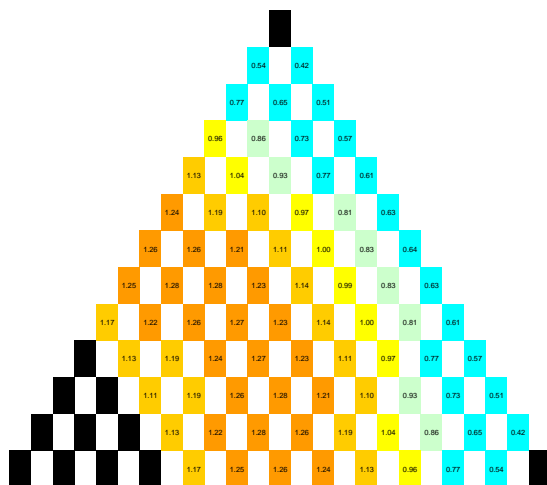
Figure 2.19. Annular Core / Uniform Enrichment – EOEC Radial Power Distribution.
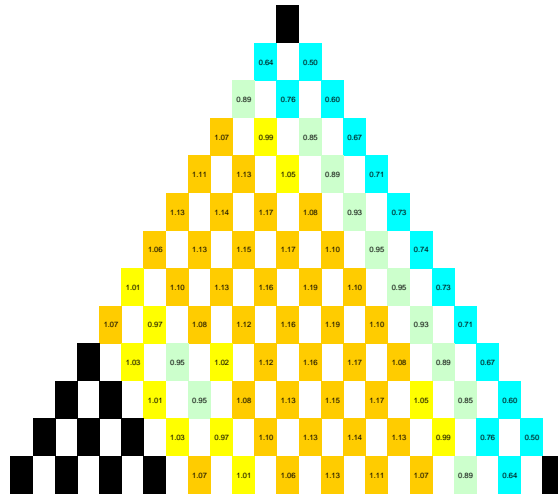
Figure 2.20. Annular Core / Non-uniform Enrichment – BOEC Radial Power Distribution.
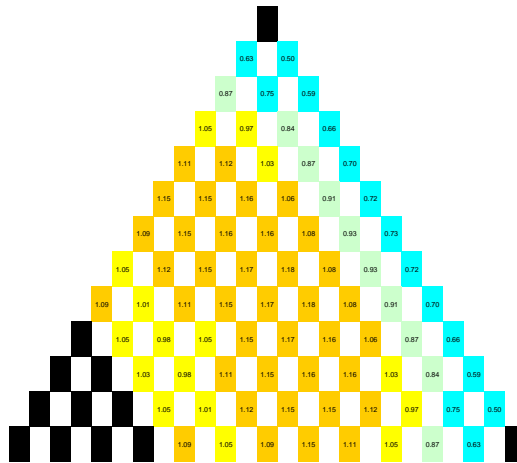
Figure 2.21. Annular Core / Non-uniform Enrichment – MOEC Radial Power Distribution.
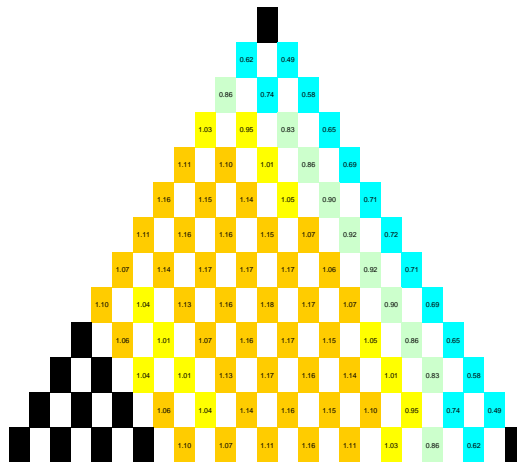
Figure 2.22. Annular Core / Non-uniform Enrichment – EOEC Radial Power Distribution.

Figure 2.23. Small 600 MWt Core – BOEC Radial Power Distribution.

Figure 2.24. Small 600 MWt Core – MOEC Radial Power Distribution.

Figure 2.25. Small 600 MWt Core – EOEC Radial Power Distribution.

2.4 Control Rod Worth and Safety Parameter Evaluation

The reference core layout with a split batch fuel loading strategy with the maximum TRU enrichment limited to 20 w/o TRU/HM was chosen for further analysis. This included the determination if sufficient control rod locations were included in the design and evaluation of a number of safety parameters. Table 2.2 includes a summary for this design. The performance is essentially unchanged from the original designs. Figure 26 shows the charge enrichment of each assembly in the split-batch design with the control and shutdown assemblies identified by bold outline.

The usual set of safety parameters were evaluated to confirm that there were no changes resulting from the enrichment splitting that could compromise the safety of the reactor. The results are included in Table 2.3. There are some significant changes from the uniform loading. The magnitude of the Doppler temperature coefficient increased by 50% and the depressurization reactivity is approximately 20% smaller relative to the uniform enrichment case.

The goal of the control rod analysis was to determine if sufficient control rod locations were included, but it was not intended to optimize the control rod design or even evaluate individual control rod worths. The methodology was to evaluate the k_{eff} of the reactor under a number of different conditions and evaluate the reactivity change based on the difference in k_{eff}. The results are provided in Table 2.4. Despite the lower core reactivity state at EOEC, the control rod worth required is actually limiting because the difference in neutron spectrum and power distribution reduces the worth of the control rods.

Natural boron in the form of B_4C was used in the available control locations. The results show that slightly less than the required reactivity is provided. The most reactive rod has nearly $1 worth of reactivity. There is clearly sufficient space allocated to the control rods because the average rod reactivity required is only $0.18. The B-10 enrichment needs to be increased in the control rods near the periphery and reduced in the centrally located control rods to increase the total reactivity of all the control rods and to spread the reactivity more uniformly among the individual control rods.

Table 2.2. Design Summary.

	Uniform	Split-Batch
Power (MWt)	2,400	2,400
Height / Diameter Ratio	0.282	0.282
Cycle Length (EFPD)	786	786
Cycles in Core	3	3
Charge Enrichment (TRU/HM)	16.5%	15-20%
Enrichment Zones	1	5
BOEC Heavy Metal Loading (MT)	56.4	56.6
EOEC Heavy Metal Loading (MT)	54.5	54.6
BOEC TRU Loading (MT)	9.6	10.3
EOEC TRU Loading (MT)	9.6	10.4
Average Discharge Burnup	10.0%	9.9%
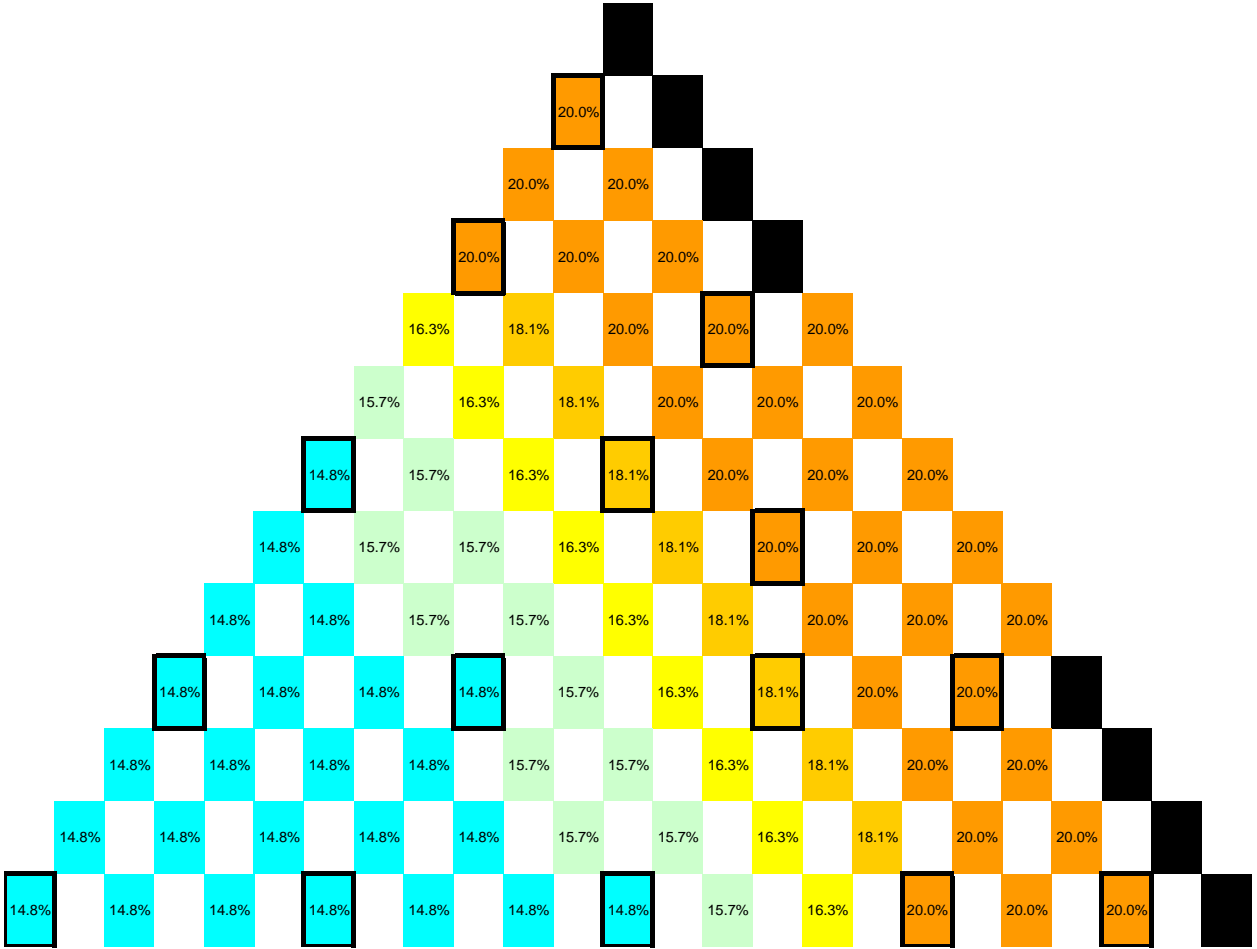
Figure 2.26. TRU Charge Enrichment for the Split-Batch Core Design.

Table 2.3. Safety Parameters.

	Uniform		Split-Batch	
	BOEC	EOEC	BOEC	EOEC
Beta	3.45E-3	3.39E-3	3.46E-3	3.40E-3
Prompt Neutron Lifetime (μsec)	2.54	2.03	2.67	2.15
Doppler Temperature Coefficient(¢/K)	-0.19	-0.17	-0.30	-0.28
Radial Expansion Coefficient ($/cm)	-0.52	-0.53	-0.42	-0.41
Axial Expansion Coefficient ($/cm)	-0.08	-0.08	-0.15	-0.13
Depressurization Reactivity ($)	1.33	1.39	1.09	1.15

Table 2.4. Control Rod Reactivity Requirements.

	BOEC	EOEC
Excess Reactivity	$0.76	$0.00
Depressurization	$1.09	$1.15
Hot-to-Cold (excludes expansion)	$4.58	$4.61
Minimum Shutdown	$2.89	$2.94
Extra Margin	$1.00	$1.00
Total Excess Reactivity Required	$10.33	$9.70
All Rods	-$11.04	-$9.56
All Rods - Minus Most Reactive Rod	-$10.06	-$8.64
Average Rod Reactivity Required	-$0.19	-$0.18
Most Reactive Rod	-$0.98	-$0.92

2.5   Conclusions

The minimum radial assembly peaking factor was estimated for a 2400 MWt, low-pressure drop (H/D=0.282) design. Very low peaking (i.e., <1.05) does not seem to be practical in this large core. The minimum peak-to-average assembly power was estimated at approximately 1.2. Split-enrichment fuel loading was most effective at reducing the radial peaking. Increased TRU enrichment of the outer assemblies was used to pull the power from the center towards the periphery. Since the core was required to maintain a conversion ratio of unity, the power redistributed over the course of a cycle. Therefore, the minimum radial peaking factor was achieved by peaking the core towards the periphery, which would lead to a flatter power distribution at the middle of the cycle and then a core that was peaked towards the center at the end of the cycle. The use of enrichment greater the 20% only allowed for relatively small improvements over the design limited to a maximum of 20%. Part of the difficulty of flattening the power distribution was a result of eliminating the breeding blankets, which are a higher quality reflector than the Zr_3Si_2 reflectors.

Fuel shuffling produces only a small improvement because the high conversion ratio produces small reactivity change over fuel lifetime. An annular core design, however gave a slightly lower peaking factor with very little power redistribution. The annular core requires a larger core diameter to accommodate the central reflector region. A small core (e.g., 600 MWt) will tend to have a much flatter radial power distribution.

The split-batch, 20% TRU enrichment limited core design was chosen for further evaluation. The performance and safety parameters were similar to that of the uniform enrichment designs. The total control rod worth for this layout was slightly low with natural boron used in all control rod locations. Using different boron enrichments in the various control rod locations should easily provide sufficient reactivity control and prevent excessive reactivity in a single control rod.

2.6   References

2.1 Toppel B. J., "A User's Guide to the REBUS-3 Fuel Cycle Analysis Capability," ANL-83-2, Argonne National Laboratory (1983).

2.2 Henryson II H., Toppel B. J., and Stenberg C. G., "MC2-2: A Code to Calculate Fast Neutron Spectra and Multigroup Cross Sections," ANL-8144, Argonne National Laboratory (1976).

2.3 Derstine K. L., "DIF3D: A Code to Solve One-, Two-, and Three-Dimensional Finite-Difference Diffusion Theory Problems," ANL-82-64, Argonne National Laboratory (1984).

2.4 Adams C. H., "Specifications for VARI3D – A Multidimensional Reactor Design Sensitivity Code," FRA-TM-74, Argonne National Laboratory (1975).

3. Fuel Pin Mechanical Design

A scoping study was performed to investigate the thermal mechanical behavior of several conceptual designs for the fuel pin. The material specified for the pin cladding was silicon carbide (SiC), which has excellent high temperature mechanical properties. The study only looked at the response of a single fuel pin attached to the support grid of a hexcan. Finite element analyses were performed for the different fuel pin configurations subjected to axial temperature variations; circumferential temperature variations were not considered at this time. For the recommended configuration, a conceptual design is proposed for the attachment of the fuel pin to the hexcan support grids.

3.1 Fuel Pin Geometry

Due to current projections of fabrication restrictions on long SiC tubing, and the required length of the fuel pin, the fuel pin is assumed to be made in two 1.67 m long sections as shown in Figure 3.1. The two-piece fuel pin will also be referred to as the two pin design, as each piece will be capped at both ends.
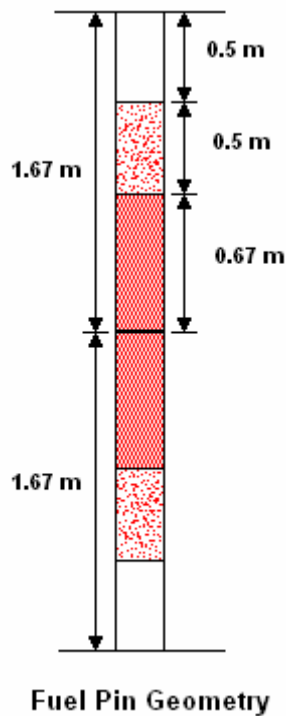
Fuel Pin Geometry

Figure 3.1 Fuel pin geometry

The upper and lower sections of the two-piece fuel pin are essentially identical, i.e., mirror images. The top of the upper fuel pin section is a 0.5 m long upper axial fission gas plenum, below which there is a 0.5 m long upper axial reflector. The lower portion of the upper fuel pin section contains a 0.67 m length of fuel pellets that when combined with the 0.67 m upper portion of the lower fuel pin section forms the 1.34 m active core

length. The lower portion of the lower fuel pin section forms a 0.5 m lower axial reflector length and a 0.5 m lower axial fission gas plenum length. The fuel pin outside diameter is 0.957 cm and the fuel clad thickness is 0.1 cm.

3.2 Fuel Pin and Hexcan Temperature Distributions

Data was provided for the axial temperature distribution in the active core region of the fuel pin. The coolant temperature at the inlet is given as 485 ºC. From this data, the temperature at the bottom of the fuel pin is assumed to equal the inlet coolant temperature, and the axial temperature in the lower portion of the fuel pin is assumed to vary linearly through the plenum and reflector until the temperature of the bottom of the active core region is reached. The axial temperature distribution in the "unheated" upper reflector and plenum regions is assumed to vary linearly from the temperature at the top of the active core region, 993.58 ºC, to approximately 915 ºC. This is basically the bulk coolant outlet temperature. The axial temperature profile of the fuel pin is shown in Figure 3.2. The fuel pin temperature was assumed to be constant in the circumferential direction.

The axial temperature profile assumed for the hexcan (Figure 3.2) is dictated by the temperature of the fuel pin at its endpoints, where the fuel pin is attached to the hexcan. Essentially, the hexcan, which is unheated, follows the coolant temperature profile up the flow channel. The hexcan temperature was assumed to be constant in the circumferential direction also.
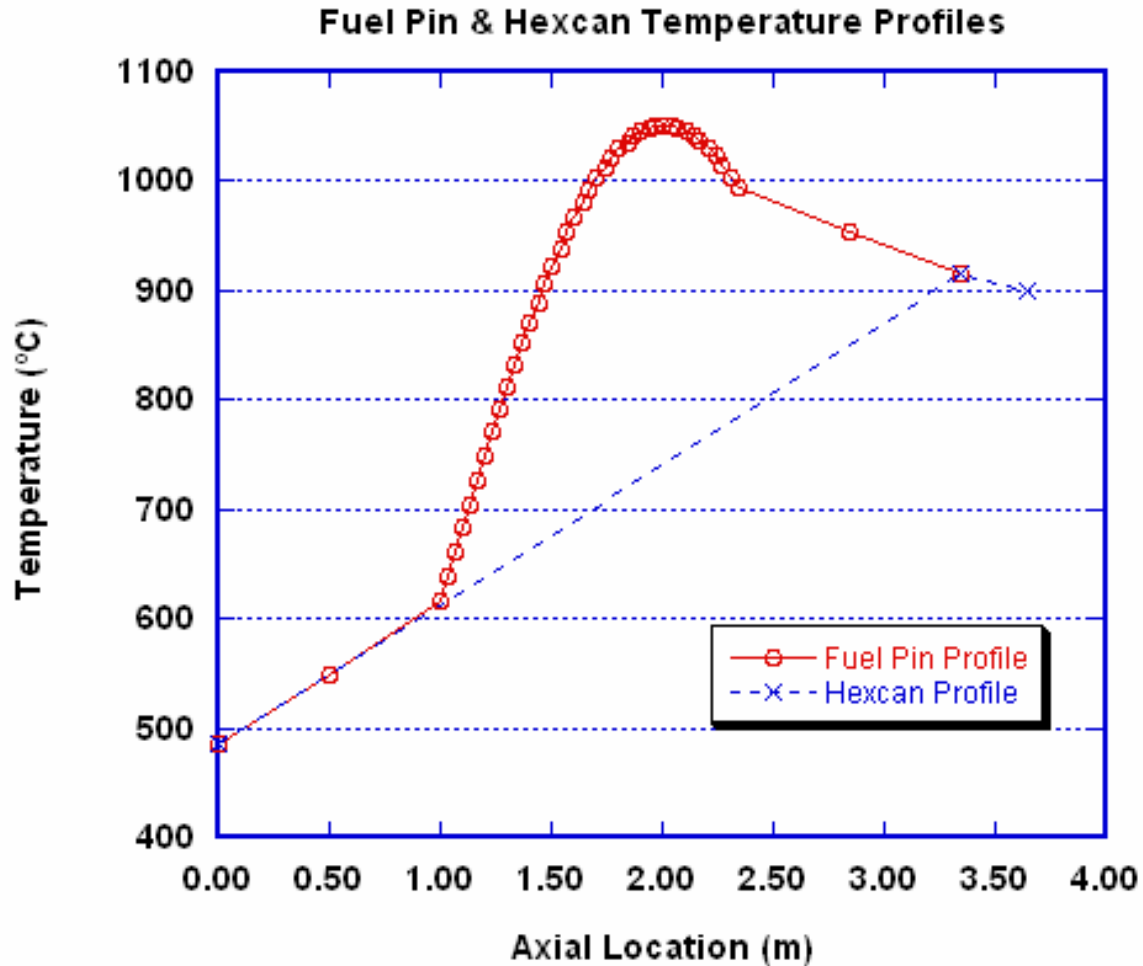
Figure 3.2 Fuel pin and hexcan axial temperature profiles

3.3 Fuel Pin Material Properties

The fuel pin clad is made of SiC. The properties of bulk SiC used in the finite element analysis are:

- Elastic Modulus: 460 GPa
- Density: 3.25 g/cm^3
- Coefficient of Thermal Expansion: 4.0 x 10^{-6}/°C
- Poisson's Ratio: 0.18
- Tensile Strength: 100 MPa
- Flexural Strength (@RT): 700 MPa
- Compressive Strength (@RT): 4.6 GPa

It should be noted that from a theoretical consideration, the flexural strength should be equal to the tensile strength. However, it has been observed that for brittle materials, which are sensitive to surface flaws, these two values are usually not equal. Thus, the lower valued tensile strength could be considered a lower bound value for failure, and the flexural strength as the most probable value for failure in bending.

23

3.4 Fuel Pin Structural Analysis Configurations

Six fuel pin configurations were examined using finite element analysis. In four of the six cases, the two-piece fuel pin was modeled as a single piece fuel pin. This simplification presupposes that the two sections of the fuel pin can be joined in such a way to form one contiguous length of material, or that a method can be found to form full length SiC fuel pins. Also in four of the six cases, the effect of connecting and constraining the fuel pin within a hexcan is introduced.

3.4.1 Case 1: One-piece simply supported fuel pin

This configuration represents the simplest case possible (Figure 3.3). The ends of the fuel pin are constrained so as to restrict translational motion only. The ends of the fuel pin will be attached to the fuel support plates. A translational constraint in the i-th coordinate direction is denoted by T_i, and a rotational constraint about the i-th coordinate axis is denoted by R_i. Thus, T_{xyz} indicates that the point is constrained from motion in the x, y and z directions, and R_x indicates that rotation about the **x**-axis is constrained. This is the case of a fuel bundle with no spacer grids.

Figure 3.3 Case 1: One-piece simply supported fuel pin

3.4.2 Case 2: Two-piece fuel pin with ends simply supported and center fixed

This configuration represents the case of two fuel pins joined together with all motion restricted at the connection (Figure 3.4). This is the case of a fuel bundle design with a single fuel support grid at the midplane of the fuel pins.
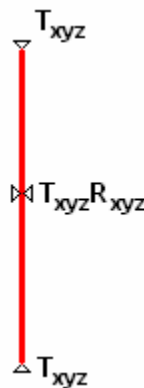
Figure 3.4 Case 2: Two-piece simply supported fuel pin with center fixed

24

3.4.3 Case 3: One-piece fuel pin within hexcan

Case 3 introduces the effects of the hexcan in constraining the fuel pin (Figure 3.5). The lower end of the fuel pin and hexcan are joined and simply supported. The upper end of the hexcan is simply supported and allowed to move in the axial direction, while the upper end of the fuel pin is joined to the hexcan and is thus constrained to move with the hexcan. The top and bottom fuel support grids provide the structural attachment. This model takes into account the axial thermal expansion of the hexcan
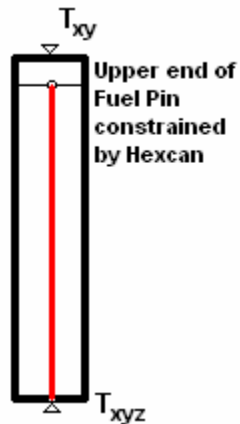
Figure 3.5 Case 3: One-piece fuel pin within hexcan

3.4.4 Case 4: One-piece fuel pin and single spacer within hexcan

Case 4 is identical to Case 3 with the addition of a single spacer centered axially along the fuel pin (Figure 3.6). The spacer restricts the fuel pin from moving laterally within the hexcan but allows for axial motion likely to occur due to thermal expansion.
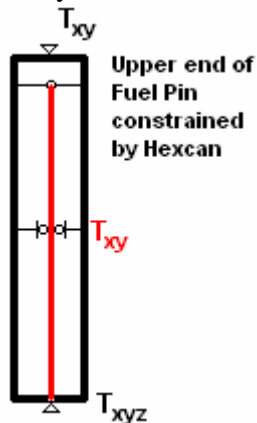
Figure 3.6 Case 4: One-piece fuel pin and single spacer within hexcan

3.4.5 Case 5: One-piece fuel pin and three spacers within hexcan

Case 5 expands on Case 4 by adding two more spacers located at the ends of the active core of the fuel pin (Figure 3.7). The spacers restrict fuel pin lateral movement while allowing for axial motion likely to occur due to thermal expansion.
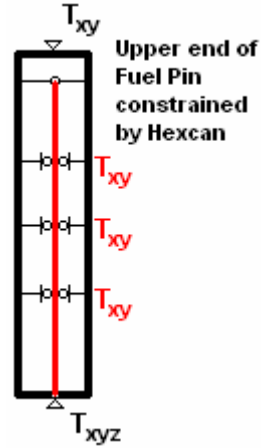
Figure 3.7 Case 5: One-piece fuel pin and three spacers within hexcan

3.4.6 Case 6: Two-piece fuel pin fixed to the hexcan at the center support grid with ends free to expand axially

Case 6 introduces a conceptual design for the attachment of the fuel pin to the hexcan supports to mitigate thermal stresses developed and minimize lateral bowing of the fuel pin (Figure 3.8). A two-piece fuel pin is rigidly attached to the hexcan so the ends of the two fuel pin sections are joined at the axial center of the hexcan with the center support grid (Figure 3.9). The other ends of the two fuel pin sections are constrained to prevent lateral motion but are allowed to translate axially to accommodate thermal expansion (Figure 3.10).
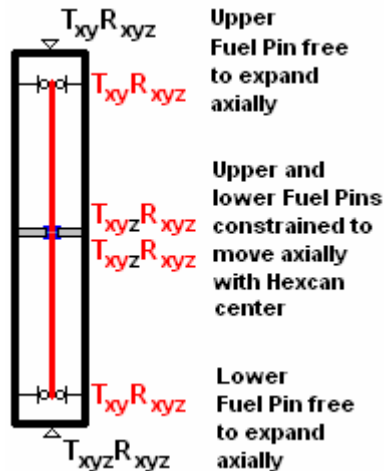
Figure 3.8 Case 6: Two-piece fuel pin with free ends and centers fixed to hexcan

26
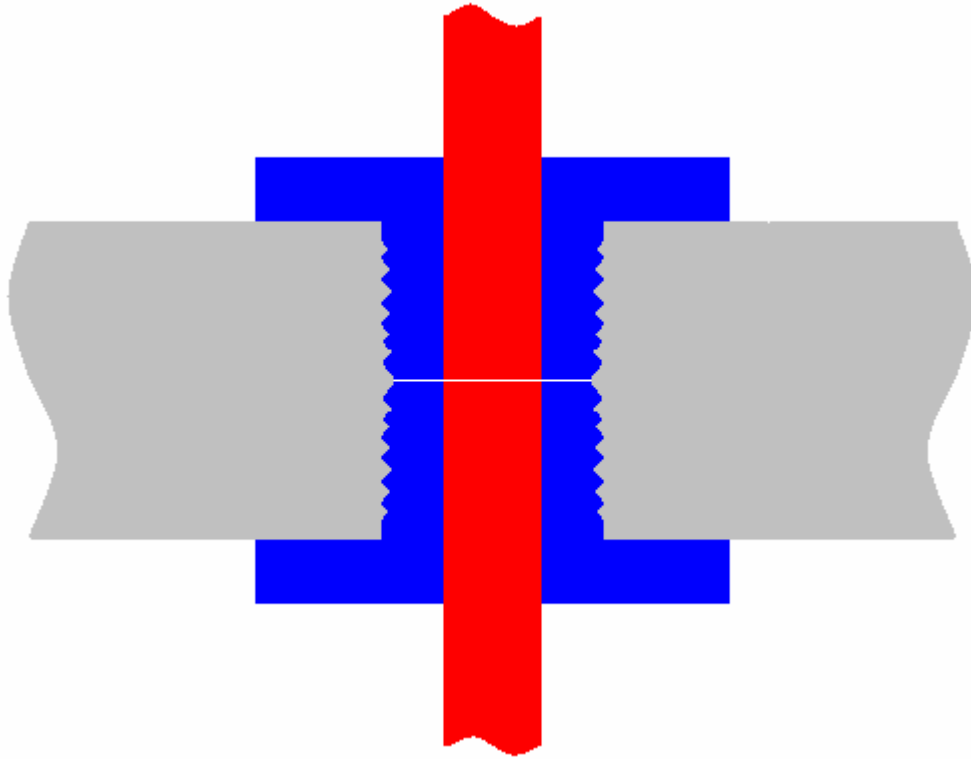
Figure 3.9 Conceptual design for fuel pin attachment to center support grid
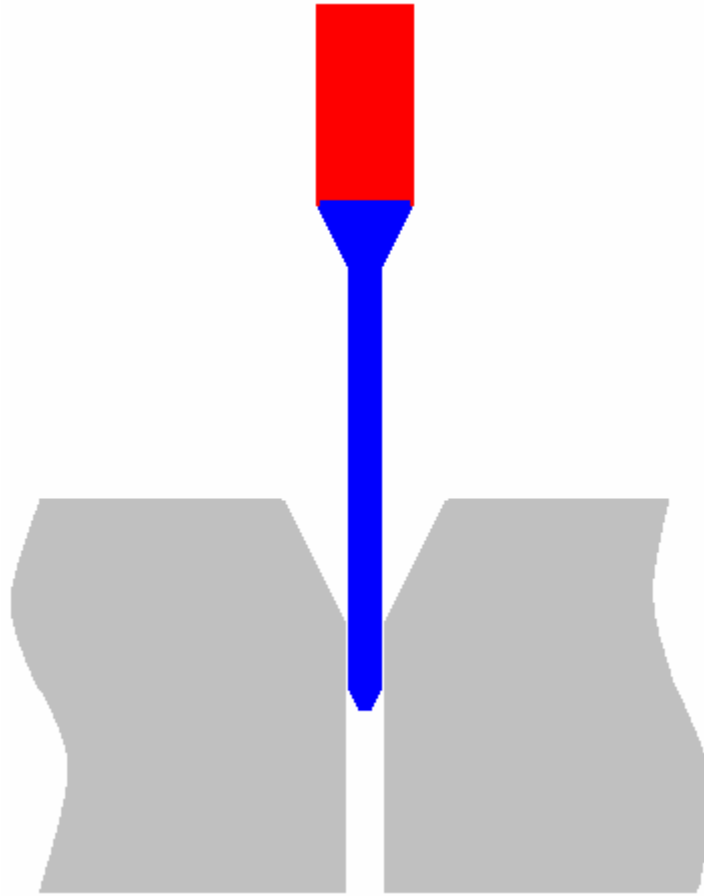
Figure 3.10 Conceptual design for fuel pin end support

3.5 Fuel Pin Analysis Displacement Results

Finite element analyses were performed for each configuration and lateral displacement, or bowing, of the fuel pin was examined. In order to initiate the lateral displacement, the fuel pin was modeled with a very slight imperfection. This is reasonable because the manufacturing process would not produce a perfectly straight fuel pin. The chosen imperfection was a sinusoidal shape with a maximum lateral displacement of 0.01 cm at its axial midpoint.

3.5.1 Case 1: One-piece simply supported fuel pin

This case exhibited the greatest amount of fuel pin lateral displacement. A maximum lateral displacement of 7.8 cm was calculated for the axial midpoint of the fuel pin (Figure 3.11).
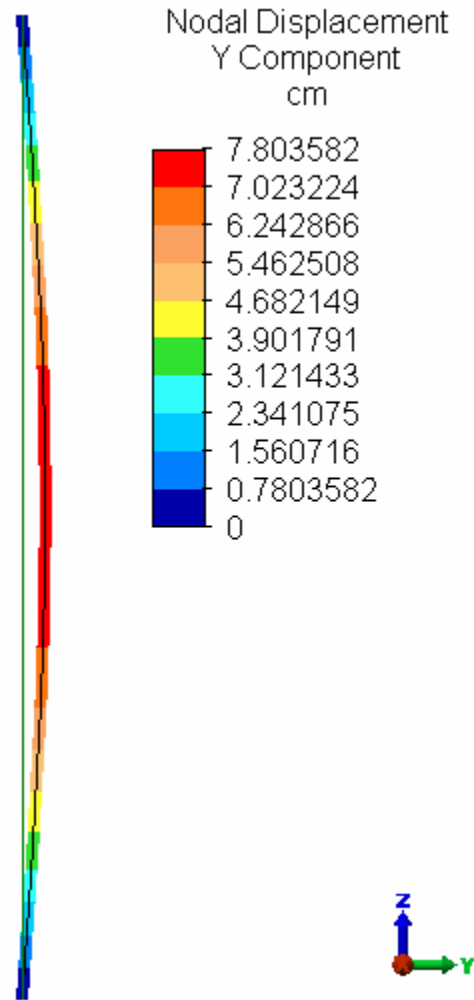
Figure 3.11 Case 1 fuel pin lateral displacement

3.5.2 Case 2: Two-piece fuel pin with ends simply supported and center fixed
The maximum lateral displacement of the fuel pin for Case 2 is approximately 4.5 cm and occurs near the axial midpoint of the upper section of the two-piece fuel pin (Figure 3.12). It should be noted that this behavior agrees with intuition. Since the temperatures are higher in the upper section of the fuel pin, it is expected that the upper section of the fuel pin will expand more than the lower section, and as a result, will experience greater lateral displacement.
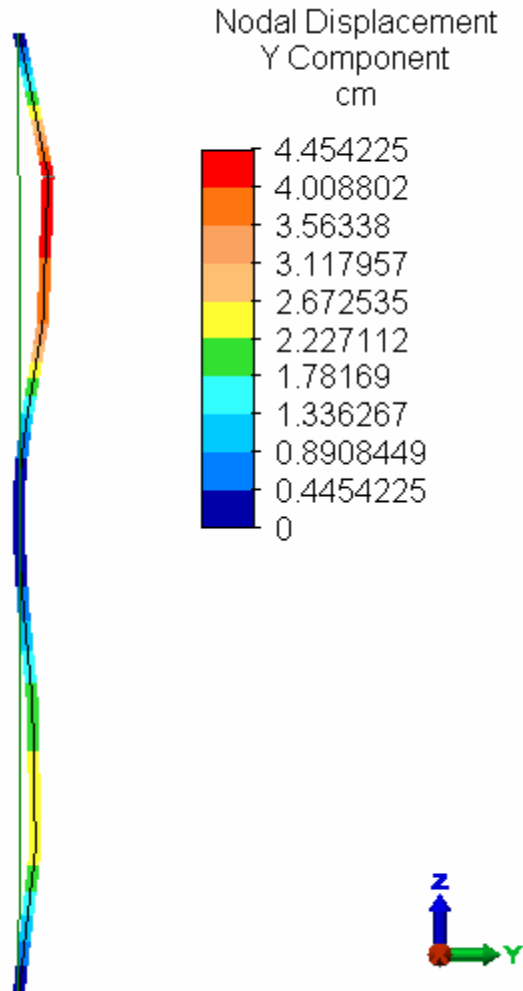
Figure 3.12 Case 2 fuel pin lateral displacement

3.5.3 Case 3: One-piece fuel pin within hexcan

The lateral displacement of the fuel pin for Case 3 is mitigated due to the effect of the hexcan (Figure 3.13). The hexcan temperatures are not as high as those experienced by the fuel pin, so the hexcan does not lengthen as much due to thermal expansion as the unrestrained fuel pin would. The upper end of the fuel pin is constrained to move with the hexcan. In this configuration, the unrestrained axial midpoint of the fuel pin experiences a maximum lateral displacement of 4.6 cm, an amount 41% less than the 7.8 cm bowing predicted for Case 1, which did not move axially.
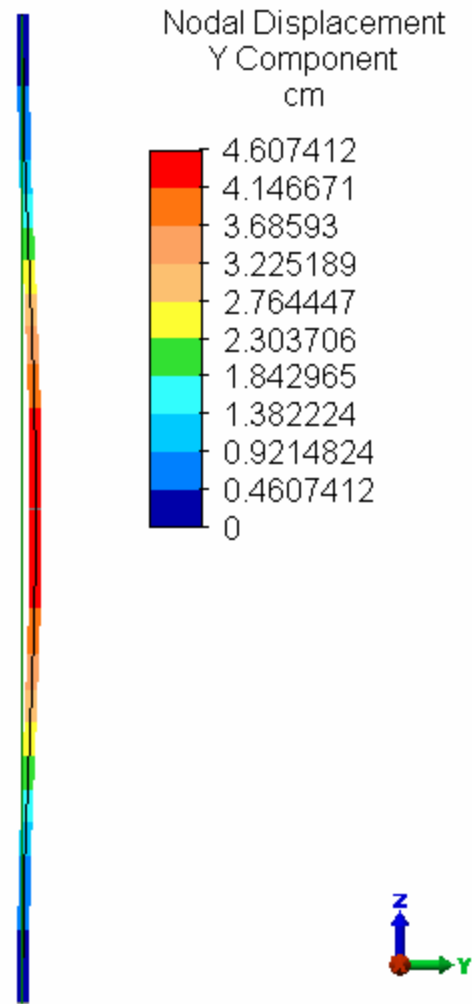
Figure 3.13 Case 3 fuel pin lateral displacement

3.5.4 Case 4: One-piece fuel pin and single spacer within hexcan

The single spacer restricts lateral displacement of the fuel pin at its axial midpoint. The maximum lateral displacement is approximately 2.18 cm and occurs in the upper portion of the fuel pin (Figure 3.14). The maximum lateral displacement in the lower portion of the fuel pin is only slightly less at 2.17 cm.
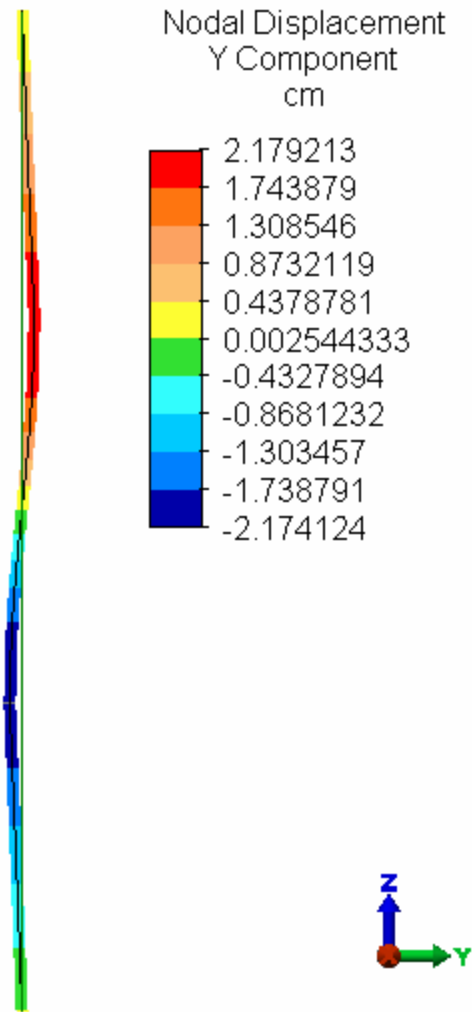
Figure 3.14 Case 4 fuel pin lateral displacement

3.5.5 Case 5: One-piece fuel pin and three spacers within hexcan

Three spacers restrict lateral displacement of the fuel pin at additional locations. The maximum lateral displacement for Case 5 is approximately 1.0 cm and occurs in the upper portion of the fuel pin in the region above the upper spacer (Figure 3.15). The maximum lateral displacement in the lower portion of the fuel pin below the lower spacer is only slightly less at 0.99 cm.
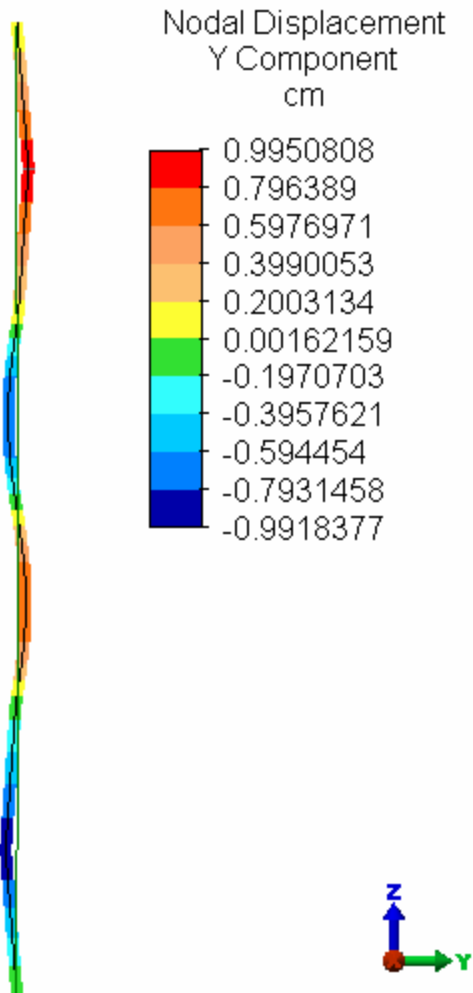
Figure 3.15 Case 5 fuel pin lateral displacement

3.5.6 Case 6: Two-piece fuel pin fixed to hexcan at center support grid with ends free to expand axially

Case 6 exhibits no appreciable lateral displacement. The upper and lower ends of the two-piece fuel pin are free to expand axially, while the middle of the fuel pin is constrained to move with the hexcan. The axial displacement of the fuel pin in this configuration is given in Figure 3.16.
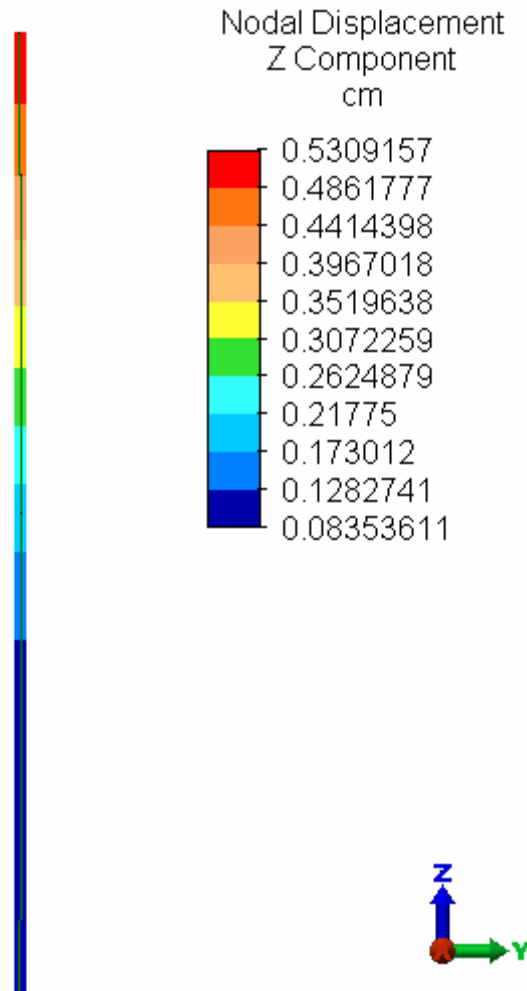
Figure 3.16 Case 6 fuel pin axial displacement

3.6 Fuel Pin Structural Analysis Results Summary

In addition to fuel pin displacements, axial forces and stresses that develop within the fuel pin due to the thermal loading are examined. The axial force developed is compared to the critical buckling force calculated for each case except Case 6. No compressive axial force develops in Case 6 since the ends of the fuel pin are free to expand axially.

The critical buckling load, P_{cr}, depends on the geometric end conditions of the fuel pin and is calculated using the following equation:

$$P_{cr} = \frac{\pi^2 EI}{(KL)^2} \tag{2-1}$$

where, E is the elastic modulus of the material, I is the moment of inertia of the fuel pin cross section, L is the length of the fuel pin, and K is a dimensionless coefficient dependent on the geometric end conditions [Budynas, 1977]. For the configurations of Case 1 and Case 3, $L = 3.34$ m and $K = 1.0$. For the configuration of Case 2, $L = 1.67$ m and $K = 0.7$. In Case 4, $L = 1.67$ m and $K = 1.0$. In Case 5, $K = 1.0$ and $L = 0.67$ m.

The fuel pin structural analysis results for all six cases are summarized in Table 3.1.

Table 3.1. Summary of fuel pin structural analyses

Fuel Pin Configuration	Steady State Compressive Axial Force in Fuel Pin (Newtons)	Fuel Pin Critical Buckling Force (Newtons)	Maximum Compressive Stress in Fuel Pin (MPa)	Maximum Tensile Stress in Fuel Pin (MPa)	Fuel Pin Bowing (cm)	Fuel Pin Axial Expansion (cm)
1) Simply Supported Fuel Pin	102.5	102	158	149	7.8	n/a
2) Two Pins fixed at center joint and pinned at ends	930 (both upper and lower pins)	833	36.2 (upper pin) 35.5 (lower pin)	No Tensile Stress: Compressive axial stresses dominate bending tensile stresses	4.45 (upper pin) 2.53 (lower pin)	n/a
3) One Fuel Pin w/ HexCan	422	102	205	173	4.6	0.29
4) One Fuel Pin w/ HexCan and 1 spacer grid	891	408	306	240	2.2	0.29
5) One Fuel Pin w/ HexCan and 3 spacer grids	2890	2540	538	324	1.0	0.29
6) 2 Fuel Pins attached to HexCan center support grid, ends free to expand	n/a	n/a	0.000912 (upper pin) 0.000193 (lower pin)	0.000912 (upper pin) 0.000193 (lower pin)	~0	0.33 (upper pin) 0.12 (lower pin)

3.7 Summary and Conclusions

A scoping study was performed to gain insight into the thermal mechanical behavior of the fuel pin when subjected to axial thermal gradients. No circumferential thermal gradients were considered here. The response of only a single pin was modeled; interactions with adjacent pins will be considered in future work. Some of the models included the thermal mechanical response of the hexcan because the hexcan will see different axial temperature gradients. A potential design for a split fuel pin was developed that did not develop significant stresses or bowing under only axial temperature gradients.

Six fuel pin configurations were examined to determine their thermal mechanical behavior when subjected to an axial temperature variation.

- Because of the differential thermal expansion between the hexcan and fuel pin, five configurations developed compressive forces that exceed the critical buckling force. However, this is of no consequence because the fuel pin is not a structural element and, thus, would not collapse.
- Four configurations developed tensile stresses that exceed the tensile strength of the material but do not exceed the flexural strength. The compressive strength of the material was far from being reached.
- Five configurations led to measurable lateral displacement, or bowing, of the fuel pin. Constraints imposed by adjacent fuel pins, which were not considered here, would reduce bowing.
- One configuration (Case 6) avoided developing significant forces and stresses in the fuel pin, and did not exhibit appreciable bowing.

It is recommended that the configuration for Case 6 should be considered for further evaluation in the initial design of the Generation IV Advanced Gas Cooled Reactor.

3.8   References

3.1 Budynas R.G., Advanced Strength and Applied Stress Analysis, McGraw-Hill, Inc., New York, 1977.

4. Subassembly Thermal-Hydraulic Design

The 2400 MWt Gas Fast Reactor (GFR), which is being developed, uses helium at 70 bars as the primary coolant. It is a direct-cycle reactor, which has the turbine included in the primary loop. During normal shutdown conditions, there is a powered shutdown heat removal system to extract the decay heat and maintain safe temperatures within the reactor core. This memo addresses an abnormal (emergency) shutdown condition where it is assumed that there are no available power sources to drive a compressor. For this situation the plant is to have emergency heat exchangers (EHXs) that are connected via piping in series with the reactor core, Figure 4.1. During normal reactor operation, check valves isolate the EHXs from the primary loop. When the EHXs are needed, the check valves open and the core and emergency heat exchangers are part of a closed flow loop. A supply of cold water is used to directly or indirectly cool the secondary side of the EHXs. This heat extraction cools the helium as it passes through the EHXs. Natural circulation drives the helium flow, which is heated as it passes up through the reactor core and cooled as it passes down through the EHXs. An important parameter is the helium pressure in the EHX loop, which will be much less than 70 bars when the EHXs are needed to cool the core. As this pressure decreases, the amount of coolant in the loop decreases along with the ability of the coolant to circulate and extract heat. It is essential that the behavior of this loop and its thermal-hydraulic limitations be well understood. Decay heat removal in the natural circulation in the helium-cooled loop formed with the reactor core in the hot leg and the emergency heat exchangers in the cold leg, Figure 4.1, is studied.   The friction pressure drop and the buoyancy pressure rise are studied separately so that greater insight into the behavior of the system can be obtained. It is observed that a fixed decay power level and system pressure in some instances can result in two possible steady states—one at a relatively high flow rate and low reactor coolant outlet temperature and another at a very low flow rate with very high reactor coolant outlet temperature. It is also observed that when the system pressure is too low, there may be no steady state condition for the system. Hence, a thorough understanding of this thermal-hydraulic behavior is essential in order to develop an effective subassembly thermal-hydraulic design.

4.1 Subassembly Geometry

Table 4.1 shows the current fuel bundle design. This bundle design is an evolution from the one detailed in [4.1]. Improvements were made in the modeling of the fuel pin gap conductance which resulted in a need to reduce the gap size. Table 4.1 shows that gap size is now 0.1 mm and there is now a central pellet hole of diameter 3.02 mm. The smeared pellet density remains what it was in Ref. 4.1.   Ref. [4.1] discusses some of the fuel performance related issues, but Table 4.1 shows that the fuel and cladding temperatures are not violated. At this stage of the design, the design margins to the various design limits are now beginning to be evaluated. The key is still the focus on the passive safety case for the depressurized decay heat removal accidents with concurrent total loss of a/c power. The major limit on the guard containment design backup pressure margin has essentially been established in the design process on the core pressure drop

margin which is a major pressure loss in the primary coolant circuit. One of the key elements in the core pressure drop loss is due to the pressure drop loss is due to the pressure drop through the core spacers. The margin on the guard containment backup pressure can be related to the number and design of the spacers utilized in the core to provide rigidity to the pin bundle. To study this aspect of the pin bundle design, chapter 3 details the pin thermal bowing performance established by the spacer requirements of the thermal-hydraulic performance of the bundle detailed below.

Table 4.1 T-H Characteristics 2400MWt Pin Bundle

2400 MWt Pin Core	
(U,Pu)C	
T-H Parameters	
Reactor power, MWt	2400
Core power density, MW/m3	100
Core inlet temperature, C	480
Core outlet temperature, C	850
System pressure, MPa	7
Core pressure drop (excluding acceleration), bar	0.54
Peak Clad temperature, C	1044
Spacer pressure drop, Pa	12170
Friction pressure drop, Pa	38094
Acceleration pressure drop, Pa	3324
Inlet pressure drop, Pa	1691
Outlet pressure drop, Pa	1802
Fuel Assembly Geometry	
Flat-to-flat of hexagonal duct (outside), mm	215
Duct wall thickness, mm	3.7
Interassembly gap,mm	7
Number of pins per core subassembly	271
Number of rings (excluding center one)	9
Number of spacers	3
Hydraulic diameter, mm	8.60
Pin pitch (average), mm	12.6
Fuel Pin Geometry	
Total pin length, m	3.34
Fuel pellet outer diameter, mm	7.37
Fuel pellet inner diameter, mm	3.02
Fuel clad thickness, mm	1.0
Fuel pin diameter, mm	9.57

4.2 Analytical Model

A good understanding of the thermal-hydraulic behavior of the EHX loop can be obtained from relatively simple steady-state models that are easy to solve on a computer spreadsheet. In the modeling it is assumed that primary coolant temperature exiting the EHXs is a known value of either 50 or 100º C. This assumption helps to keep the model simple by avoiding the need to include the secondary-side coolant of the EHXs. Since all of the emergency heat exchangers are in parallel, in the model they are assumed to be combined to form one large heat exchanger. For simplicity, in Figure 4.1 the check valves are not shown. Each fuel pin has a region below the core that includes the lower reflector and a region above the core that includes the upper reflector. The core generates a significant amount of heat, but the regions above and below it do not and are modeled as regions that do not generate heat.

There are two basic equations that must be solved to analyze the primary-side EHX loop. The first, the energy balance equation, mathematically requires that the power generated in the core (which is the same as that extracted by the EHXs) is the product of the core temperature rise, the helium flow rate, and the specific heat capacitance of the helium coolant. The second, the momentum balance equation, requires that the friction pressure drop and the buoyancy pressure rise around the loop must be equal. The friction pressure drop is due to hydraulic resistance in the core pin bundle, the parallel EHXs, and connection piping, plena, and valves. The hydraulic resistances of the latter three are not modeled. It is assumed that they can be made sufficiently small by making their flow areas sufficiently large. In future analyses theses losses can be approximated by increasing the entrance and exit losses of the pin bundle and the EHXs. The buoyancy pressure rise is due to the helium in the downward flow through the EHXs and the piping below it being denser than the upward flow through the core, the pin region above the core, and the reactor regions and the piping above the fuel pins. The greater the vertical separation between the core and the EHXs the greater is the buoyancy pressure rise. Table 4.2 shows some of the key parameters and the values of them that were used in the model.
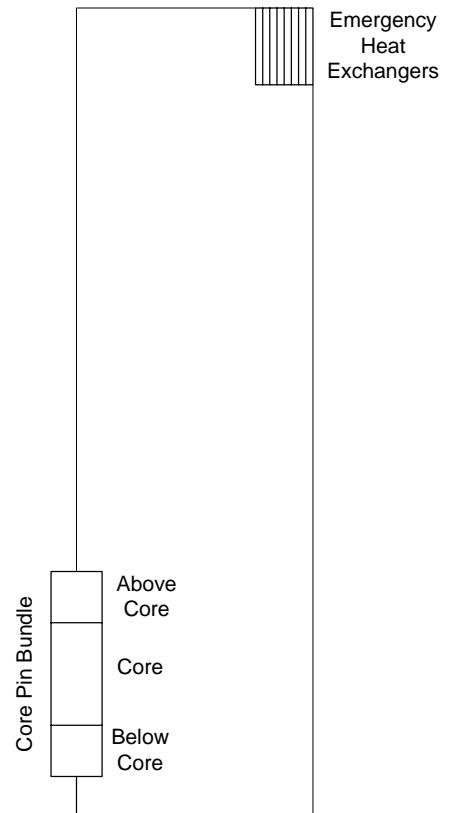
Fig. 4.1 Emergency Heat Exchanger
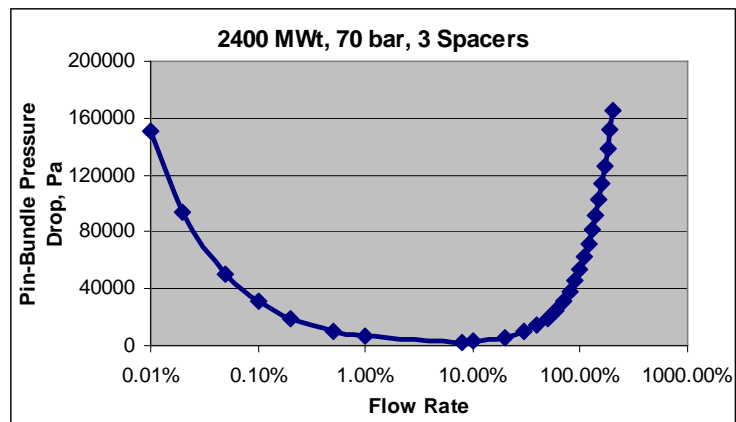
4.3 Results and Discussion

Figure 4.2 shows the core pin-bundle pressure drop as a function of flow rate with the power held constant at the normal operating power of 2400 MWt. The reactor operating inlet temperature is 480º C and the normal reactor outlet temperature (at 100% power and flow) is 850º C. When the flow rate is at a very small value the reactor outlet

temperature, as indicated by the dashed curve in Figure 4.2, is extremely high. The shape of the pressure drop curve between about 10% flow and 200% is what one would expect with pressure drop increasing monotonically with flow. However, a minimum of 2686 Pa is observed at 7.87% flow and the pressure drop rises substantial as much lower flow rates are achieved. In this flow region the flow is laminar and the pressure drop is directly proportion

Table 4.2 Key Parameters

Length above core, m	1.00
Core length, m	1.34
Length below core, m	1.00
Distance from top of pins to top of EHXs, m	13.45
Pin-bundle hydraulic diameter, cm	0.8604
Pin-bundle flow area, m^2	7.18
EHX hydraulic diameter, cm	0.3055
EHX length, m	0.30
Combined flow area of EHXs, m^2	6.011
100% Flow Rate at 2400 MWt, kg/s	1249.4

to product of the coolant viscosity and mass flow rate (kg/s) divided by the coolant density. The very high temperatures that result from the low flow rates, cause the viscosity to be relatively high and the density to be relative low. These two together more than compensate for the relatively low flow rate and thereby cause the pressure drop to increase with decreasing flow rate.

This behavior is substantially different from that of liquid flows, where the density is only a weak function of temperature and viscosity increases with decreasing temperature. Thus, for liquids the pressure drop approaches zero as the flow approaches zero. Hence, as Figure 4.2 demonstrates, for the helium gas flow under consideration there is a minimum pressure drop of 2686 Pa at 7.87% flow. All higher pressure drops have two flow solutions, one on each branch of the curve. The temperature at the minimum pressure drop is

Figure 4.2 Core Pin-Bundle Pressure Drop (Full Power = 2400 MWt)

5181º C. Thus, if an experiment were to be performed at temperatures below this value, it is expected that the higher flow solution would be observed and if the experiment were to be performed at temperatures higher than 5181º C, the low flow solution would be maintained. Either flow rate, in theory, is stable and maintainable, once achieved. If however the temperature is near 5181º C and pressure drop is above, but near the minimum pressure drop, there may be a potential for a perturbation in the system to cause an oscillation between the two steady-state operating points.

While the full power behavior of Figure 4.2 has produced some very helpful insights, the region of greatest concern is that at decay power levels. Therefore, many analyses were performed at 0.5% of full power, 12 MWt, or near it. Since the flow rate at full power is 1249.4 kg/s, if the 370º C core temperature rise is to be maintained at 0.5% power, then the corresponding flow rate must be 0.5% of 1249.4 kg/s, or 6.247 kg/s. For convenience, when doing studies at decay heat levels, 6.247 kg/s was defined as 100% flow and 12 MWt was defined as 100% power. Figures 4.3a, 4.3b, and 4.3c employs these new definitions and are analogous to Figure 4.2, but have much lower pressure drops because of the very low flow range. The reactor inlet temperature was maintained at 480º C. Figures 4.3a, 4.3b, and 4.3c have results for 100% power (12 MWt) and for both 20% above and 20% below 100% power. In both Figures 4.2 and 4.3a the system pressure is 70 bar. The analysis of Figures 4.3a was repeated for system pressures of 10 and 5 bar, Figures 4.3b and 4.3c, respectively. A comparison of Figures 4.3a, 4.3b, and 4.3c shows that, as expected, the core pin-bundle friction pressure drop is inversely proportional to the system pressure. This is to be expected because the density of the coolant is proportional to the system pressure and the friction pressure drop for laminar flow is inversely proportional to the density of the coolant. Thus, since 5 bar is 1/14th of 70 bar, Figure 4.3c can be obtained by using Figure 4.3a and changing the values on the range of the ordinate to 0 to 700 Pa in place of 0 to 50 Pa. In the analyses of Figures 4.3a, 4.3b, and 4.3c, it was assumed that the core pin-bundle had three grid spacers. Since the flow is laminar, the increase in pressure drop due to the spacers is relatively small and several more spacers could be used without a substantial change in the results.

Figures 4.4a, 4.4b, and 4.4c are the buoyancy pressure rise counterparts of Figures 4.3a, 4.3b, and 4.3c, respectively. The outlet temperature of the EHXs, which is the inlet temperature to the reactor, is assumed to be 100º C for these buoyancy pressure rise calculations. Thus, most of the cold leg, which contains the EHXs, is at this relatively cold temperature and most of the hot leg, which contains the reactor core, is at the reactor outlet temperature. The fluid density in the cold leg is therefore significantly greater than that in the hot leg. The resultant difference in the weights of these two columns of helium produces the buoyancy force that drives the flow around the loop. Figures 4.4a, 4.4b, and 4.4c show that the gravity pressure rise increases with decreasing flow rate and approaches an asymptote as zero flow is approached. This occurs because as the flow rate decreases, the temperatures in the hot leg increase. Since density is inversely proportional to absolute temperature, a very low flow rate results in very high helium temperatures and as the flow rate approaches zero, the density of the reactor outlet coolant asymptotically approaches zero.

A comparison of Figures 4.4a, 4.4b, and 4.4c shows the effect of system pressure. Decreasing the system pressure decreases the density everywhere in the loop proportionally. Since the gravity pressure rise is directly proportional to the density, decreasing the system pressure by a factor of 14 reduces the gravity pressure rise by a factor of 14. Thus, Figure 4.4c can be produced by just changing the scale Figure 4.4a so that its range is 0 to 100 Pa instead to the 0 to 1400 Pa of Figure 4.4c.

The loop flow rate for natural circulation flows is established where the friction pressure drop and the gravity pressure drop are equal. Figures 4.5a, 4.5b, 4.5c, and 4.5d are examples where a core pin-bundle friction pressure drop and its corresponding gravity pressure rise curve are plotted on the same graph so that the points where the two are equal can be observed. Two inconsistencies between the pairs of curves in each of these four figures should be noted. First, the friction pressure drop curves include only the pin pressure drop, but not the rest of the hydraulic resistance around the loop. Second, the reactor inlet temperature is 480º C in the friction pressure drop calculations, rather than the 100º C of the gravity pressure rise ones. In spite of these flaws, which make the precise numerical results inaccurate, Figures 4.5a, 4.5b, 4.5c, and 4.5d are suitable for demonstrating a concept. Figure 4.5a and 4.5c each have two intersection points, while Figure 4.5b and 4.5d have none. Thus, the Figures 4.5a and 4.5c each have two possible flow solutions and Figure 4.5b and 4.5d have none. Increasing the system pressure in Figure 4.5b and 4.5d would lower the friction curve and raise the gravity curve. This could be done in such away as to allow the two curves to meet tangentially at a single point, or if a greater pressure were used there would be two solutions, as in the Figures 4.5a and 4.5c.

Studying the friction and gravity components of natural circulation separately is informative and provides useful insights into the behavior of the EHX loop. However, both components can be included in a single mathematical model that can be used to show the relationship between reactor coolant outlet temperature and system pressure for various decay power levels, Figure 4.6. Figure 4.6 reverts back to defining 100% power to be 2400 MWt. For this analysis the outlet temperature of the EHXs was assumed to be 50ºC and the hydraulic resistance of the EHXs was included in the calculations. Key parameters for this calculation are provided in Table 4.2, above. Decay power levels of 0.25, 0.5, 1.0, and 2.0% are considered. The lowest temperature on each curve was arbitrarily selected to be 450ºC. For each power level it is observed that as the system pressure is reduced the coolant outlet temperature increases until the point where the minimum pressure is reached. This point is represented as the highest temperature on shown each curve. As indicated in Figures 4.5a and 4.5c above, for each system pressure there can be two solutions—one with high flow and a low coolant outlet temperature and another with a low flow and a high coolant outlet temperature. Thus, each curve in Figure 4.6 could be extended to higher temperatures by including the high temperature (low flow) solutions. If this were done, for each power level curve there would be two temperatures for each pressure above the minimum. Figure 4.6 also shows that, depending on power level, a reduction of only about 1 to 4 bars in system pressure can cause the outlet coolant temperature to increase by 1000ºC or more.
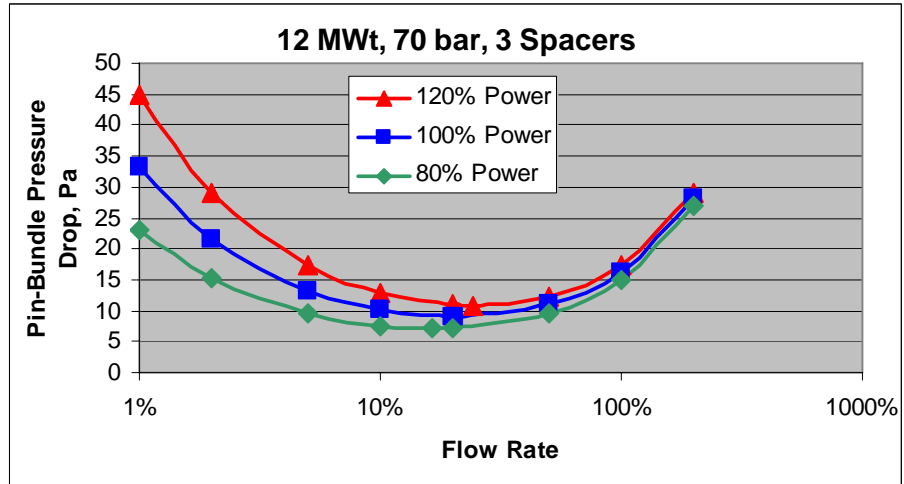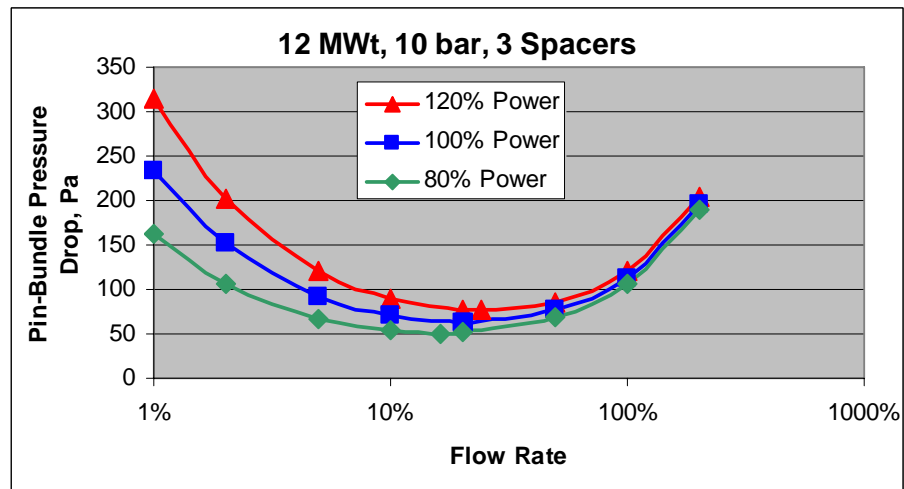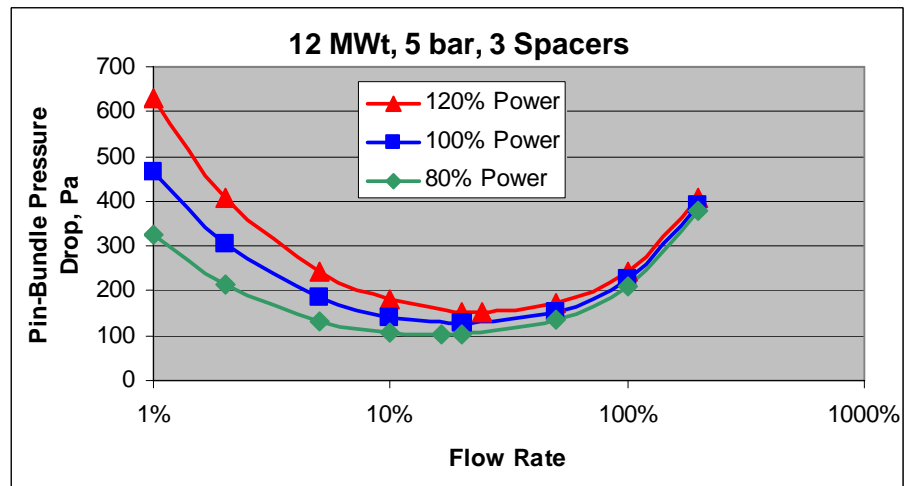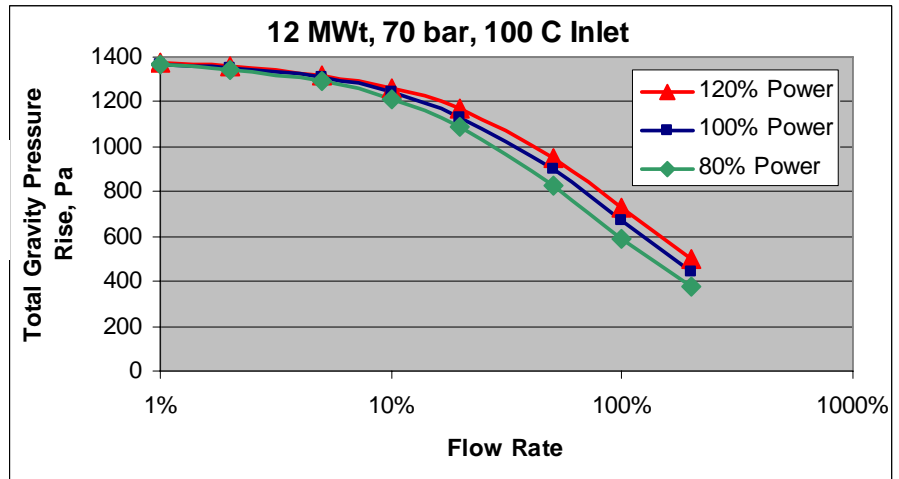
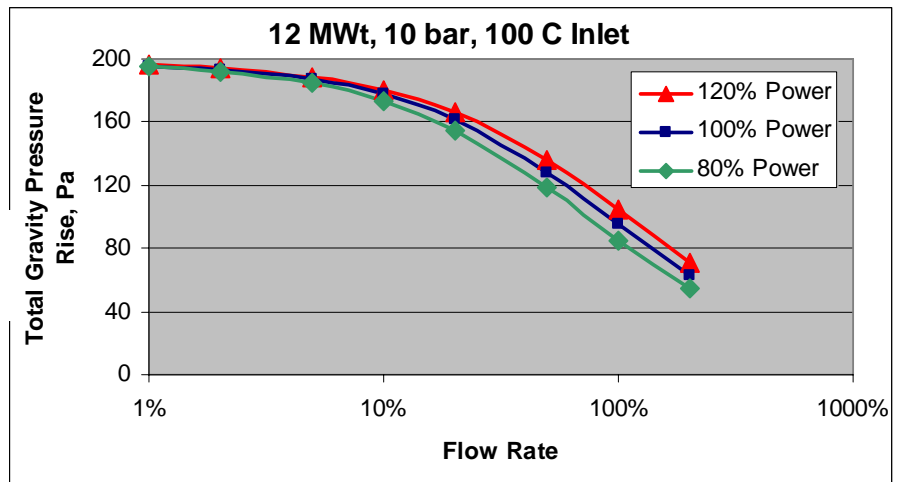Figure 4.3a
70 bar

Figure 4.3b
10 bar

Figure 4.3c
5 bar

Figures 4.3a, 4.3b, and 4.3c   Core Pin-Bundle Pressure Drop (Full Power = 12 MWt)
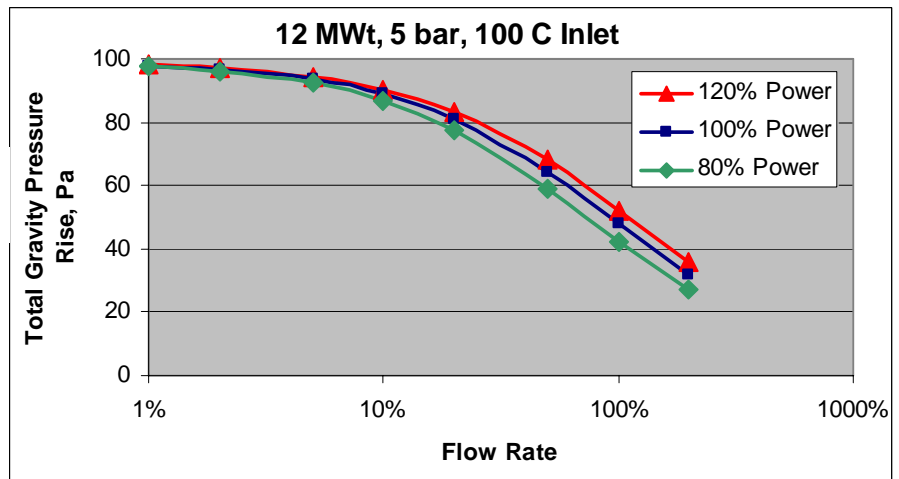
**Figure 4.4a
70 bar**

**Figure 4.4b
10 bar**

**Figure 4.4c
5 bar**

**Figures 4.4a, 4.4b, and 4.4c   EHX-Loop Gravity
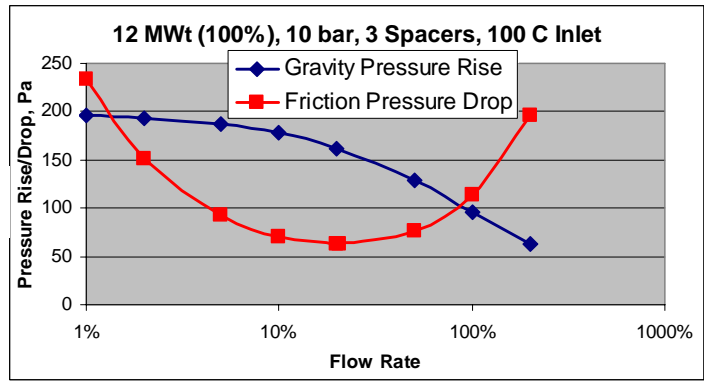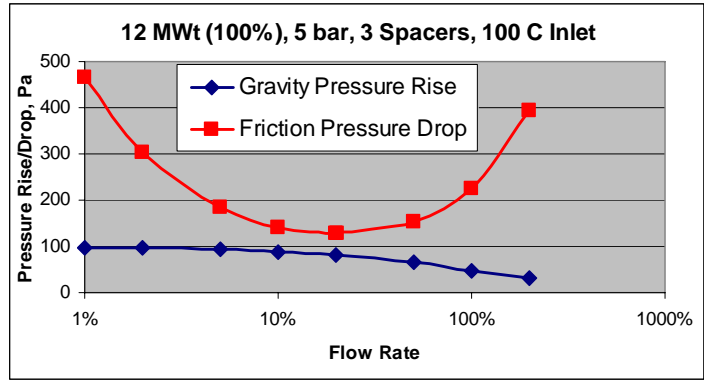Pressure Rise (Full Power = 12 MWt)**
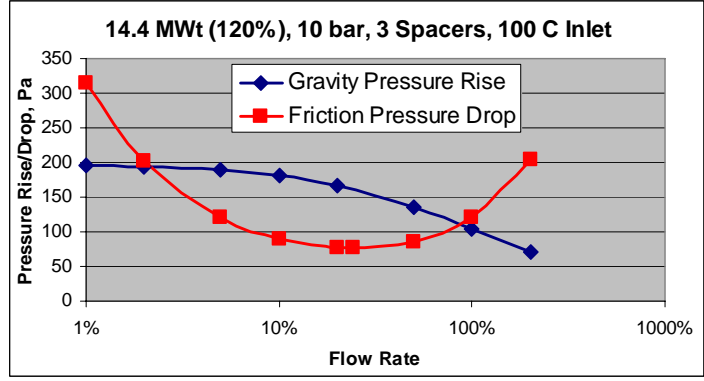
Fig. 4.5a
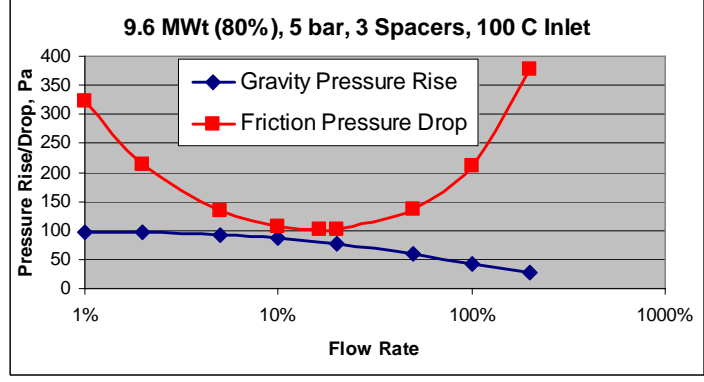
Fig. 4.5b

Fig. 4.5c

Fig. 4.5d

**Figures 4.5a, 4.5b, 4.5c, and 4.5d Equating
Friction Pressure Drop with Gravity Pressure
Rise (Full Power = 12 MWt)**

4.4 Conclusions

The behavior of natural circulation in gas-cooled system can have some unusual behaviors that are not present in liquid-cooled systems. In particular, low flows can result in *increasing* friction pressure drop with decreasing flow rate. Because of this behavior, a given system pressure drop and system pressure may have two steady-states—one at a relative high flow rate with a relatively low core outlet temperature and another at a relatively low flow rate with a relatively high core outlet temperature. It is also possible that if the system pressure is too low there may be no steady-state condition. Thus, in designing natural circulation decay heat removal systems for GFRs it is important to be able to guarantee that the system pressure in the EHX loop will always be maintained at a sufficiently high value while this system is in use.
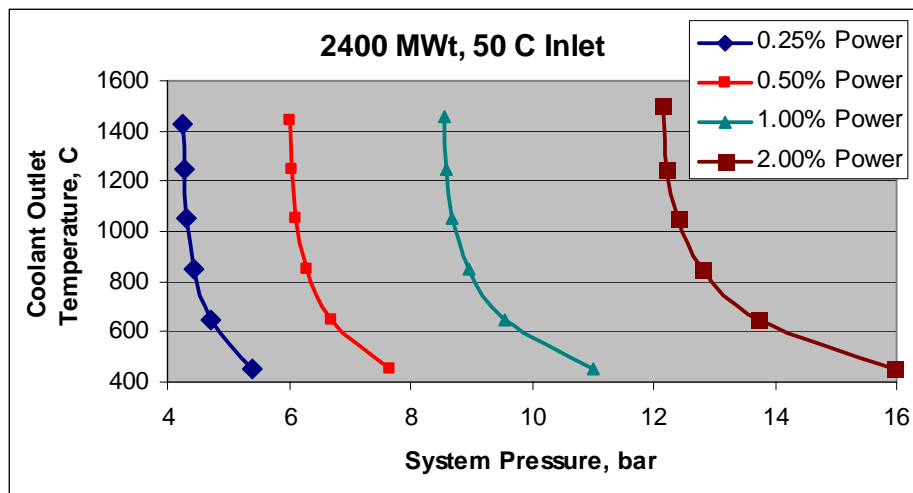
Figure 4.6 Core Coolant Outlet Temperature vs. System Pressure